EXPERIMENTAL RESPONSE OF A ROTOR SUPPORTED ON RAYLEIGH STEP GAS BEARINGS

A Thesis

by

XUEHUA ZHU

Submitted to the Office of Graduate Studies of
Texas A&M University
in partial fulfillment of the requirements for the degree of

MASTER OF SCIENCE

August 2004

Major Subject: Mechanical Engineering

EXPERIMENTAL RESPONSE OF A ROTOR SUPPORTED ON RAYLEIGH STEP GAS BEARINGS

A Thesis

by

XUEHUA ZHU

Submitted to Texas A&M University
in partial fulfillment of the requirements
for the degree of

MASTER OF SCIENCE

Approved as to style and content by:

Luis San Andrés	John Vance
(Chair of Committee)	(Member)
Othon Rediniotis	Dennis O' Neal
(Member)	(Head of Department)

August 2004

Major Subject: Mechanical Engineering

ABSTRACT

Experimental Response of a Rotor Supported on
Rayleigh Step Gas Bearings. (August 2004)
Xuehua Zhu, B.S., Xi'an Jiao Tong University
Chair of Advisory Committee: Dr. Luis San Andrés

Gas bearings enable successful applications in high speed oil-free micro-turbomachinery. This thesis presents analysis and experiments of the dynamic performance of a rotor supported on Rayleigh step gas bearings. Comprehensive experiments demonstrate that Rayleigh step hybrid gas bearings exhibit adequate stiffness and damping capability in a narrow range of shaft speeds, up to ~ 20 krpm.

Rotor coastdown responses were performed for two test bearing sets with nominal radial clearance of 25.4 μm and 38.1 μm, respectively. A near-frictionless carbon (NFC) coating was applied on the rotor to reduce friction against its bearings at liftoff and touchdown. However, the rotor still experienced dry friction at low shaft speeds (below ~ 4,000 rpm). Experiments show that the supply pressure raises the rotor critical speed and decreases the system damping ratio. The geometry of the Rayleigh steps distributed on the rotor surface generates a time varying pressure field and results in a sizable 4X super synchronous component of bearing transmitted load. The external supply gas pressure affects slightly the onset speed of instability of the rotor-bearing system. The unstable whirl frequencies are nearly fixed at the system natural frequency (~ 120 Hz).

Analysis with a finite element model predicts the stiffness and damping force coefficients for the bearing accounting for a purely hydrodynamic operation condition. Predictions show the synchronous stiffness and damping coefficients decrease with shaft speed. Predicted threshold speeds of instability are lower, ~ 50% or less than the measurement due to the analytical model limitations assuming a grooved stator. The

predicted synchronous responses to imbalance correlate well with the measurements, however.

The Rayleigh step gas bearing shows similar characteristics to the flexure pivot tilting pad bearing (FPTPB) tested in 2003. However, the test Rayleigh step gas bearings exhibit a much reduced stable operating speed range, below 20 krpm. The maximum speed achieved is much lower to that determined with an identical rotor supported on FPTPBs, i.e. rotor dynamically stable up to 100 krpm. The FPTPB is more reliable in high speed oil-free applications due to its excellent stability characteristics.

DEDICATION

To my family

ACKNOWLEDGEMENTS

I sincerely appreciate my advisor, Dr. San Andrés, for his unlimited patience, expertise and counseling. The financial support of the Turbomachinery Research Consortium is greatly acknowledged. Thanks to Meruit Inc. for providing the test bearings and Argonne National Laboratory for coating the rotor. I thank my peers at Texas A&M University Turbomachinery Laboratory for their assistance during my research.

NOMENCLATURE

a	Damping component of a rotor motion eigenvalue [N-s/m]
A, B	Rotor initial motion amplitudes [m]
C	Bearing nominal radial clearance [m]
C_f	Nominal radial clearance along the bearing circumferential direction [m]
C_e	Bearing effective damping coefficients [N-s/m]
C_{ij}	Bearing damping coefficients; $i, j = X, Y$ [N-s/m]
D	Nominal rotor diameter [m]
D_b	Bearing bore diameter [m]
e_X, e_Y	Journal eccentricity components [m]
h	Fluid film thickness [m]
K_{ij}	Bearing stiffness coefficients; $i, j = X, Y$ [N/m]
K_{eq}	Bearing equivalent stiffness coefficient [N/m]
K_e	Bearing effective stiffness coefficient [N/m]
L	Rotor axial length [mm]
m	Imbalance mass [kg]
M	Rotor mass [kg]
M_1	Half rotor mass [kg]
M_R	Half gas bearing system mass [kg]
P	Film pressure [bar]
N_n	Rotor speed at natural frequency [rpm]
N_1, N_2	Speeds corresponding to 70% peak displacement at N_n [rpm]
P_A	Ambient pressure [bar]
R	Nominal rotor radius [m]
R'	Imbalance location [m]
s	Eigenvalues of characteristics polynomials of rotor motion
T	Air temperature [K]
ρ_A	Air density at ambient pressure [kg/m^3]

X, Y, z	Inertial coordinate system
Z_{ij}	Impedance force coefficients; $i, j = X, Y$ [N/m]
ω_c	Rotor critical speed [rad/s]
Ω, ω	Rotor rotational speed and excitation frequency [rad/s]
ζ	Damping ratio at critical speed [-]
θ	Circumferential coordinate [rad]
u	Imbalance displacement [m]
U_1, U_2	Calibrated imbalance displacements [m]
μ	Gas viscosity [Pa-s]

TABLE OF CONTENTS

Page

LIST OF FIGURES

FIGURE Page

FIGURE Page

FIGURE Page

LIST OF TABLES

INTRODUCTION

Micro-turbomachinery demands gas bearings to ensure compactness, lightweight and extreme temperature operation [1, 2]. Gas film bearings, unlike oil-lubricated bearings, offer advantages of low friction and less heat generation. These advantages have enabled their successful applications in air-cycle units for airplanes, high-precision instruments, auxiliary power units, and high-speed micro-turbomachinery [3, 4]. In addition, gas bearing systems do not require costly and complex sealing and lubricant circulation systems. Furthermore, these oil-free bearing applications eliminate process fluid contamination and are environmental friendly.

The main disadvantages of gas film bearings are little damping and low load capacity because of the gas inherently low viscosity. The provision of pressurized gas during start-up and shutdown periods is mandatory to overcome transient rubs between metal surfaces. External pressurization can provide supplemental stiffness for operation at all rotational speeds, hence reducing operating rotor eccentricity. Thus, a hybrid (hydrostatic/hydrodynamic) mode operation ultimately results in reduced power consumption. Incidentally, infamous disadvantages of gas bearings stem from two major kinds of instabilities [5]. One is pneumatic hammer controlled by the flow versus pressure lag in the pressurized gas feeding system. The other is a hydrodynamic instability, a self-excited motion characterized by subsynchronous (forward) whirl motions. A properly designed hybrid gas bearing system aids to minimize these two kinds of instabilities.

Wilde and San Andrés [6] describe comprehensive rotordynamic experiments conducted on a small rotor supported on three lobed hybrid gas bearings. These bearings are simple and inexpensive with static and dynamic force characteristics desirable in high-speed turbomachinery. These characteristics are adequate load support, stiffness and damping coefficients, low friction and wear during rotor startup and shutdown, and most importantly, enhanced rotordynamic stability. Zhu and San Andrés [7] investigate

---

This thesis follows the style and format of the ASME Journal of Tribology.

the dynamic forced performance of the same test rotor supported on hybrid flexure pivot - tilting pad bearings (FPTPBs). FPTPBs demonstrate stable performance and ability to carry dynamic loads up to 99 krpm (limit of the drive motor). Although the FPTPBs are mechanically complex and costlier than cylindrical plain bearings, their enhanced stability characteristics and predictable rotordynamic performance are desirable for high speed turbomachinery applications.

The present investigation focuses on Rayleigh step gas bearings. The Rayleigh step gas bearing is known for its good load capacity and cheap manufacturing. A Rayleigh step bearing distributes steps and ridges on the rotor surface to generate positive pressure; and axial grooves machined on the cylindrical shaft surface to create inward pump actions. This configuration prevents continuous pressure propagations along the circumferential direction. Axial grooves also provide sinks for the pressure accumulated by squeeze film action, which can enhance the gas film damping effects and stability [8]. A near-frictionless carbon (NFC) coating is applied on the rotor surface. It is of interest to investigate the coating life, and the coating effect on reducing friction and also enabling early rotor liftoff.

The objective of current work is to investigate experimentally the dynamic forced performance of a rotor supported on Rayleigh step gas bearings. The work concentrates on acquiring comprehensive rotor responses for the test bearings and justifying their reliability and durability for oil-free turbomachinery application. Imbalance responses with coast-down tests are obtained for various external supply gas pressures. In addition, a computational model for a two-dimensional Rayleigh step bearing is employed to predict the performance of the test bearings and to validate the experimental measurements. The numerical analysis is based on a Galerkin finite element method [9]. Bearing pressure distribution, load capacity, force coefficients and steady-state performance are predicted. Eigenvalues analysis determines the onset speeds of instability. Synchronous responses to mass imbalance are compared to the recorded responses.

LITERATURE REVIEW

Gas film bearings have attracted considerable attention since half a century ago. During the initial development, gas bearings were limited to aerospace turbo expanders, navigation systems and instrumentation tools [10, 11], where oil lubricated bearings were not applicable due to high speed or extreme temperature concerns. Their unique advantages are reduced power losses, compact system construction and long life applications. Gas bearings, however, have a very low load carrying capacity and require of minute film thickness to accomplish their intended function. Thus, their fabrication and installation tends to be expensive and time consuming. In addition, gas bearings offer little damping due to the low viscosity of the gas, and thus are not able to limit successfully rotor motions while traversing critical speeds. Furthermore, rigid surface gas bearings are prone to show a self-excited hydrodynamic instability, limiting their application to rotor speeds not exceeding twice the first natural frequency of the rotor-bearing system [5].

Rayleigh first discussed the theory of a step bearing in 1918, determining the optimum geometry with maximum load capacity for one-dimensional stepped bearings [12]. This configuration is nowadays referred as a Rayleigh step bearing. Rayleigh's description is based on a viscous incompressible fluid and an infinite length bearing. Auloge et al. [13] study the optimum design of step bearings with non-Newtonian lubricants. Relationships between step location and height along with a non-Newtonian parameter (correlating viscosity and shear stress) are determined and compared to classical Rayleigh step bearings. Archibald and Hamrock [14] employ a linearization method on the Reynolds equation to obtain the optimum load and friction torque of a Rayleigh step bearing of finite length. Each pad of the bearing acts independently as the pressure profile is broken at the supply grooves between the pads. However, the model is simplified with the assumption of identical film thickness in each ridge and step region, resulting in discrepancies with measurements. Hamrock [15] improves his early analysis by considering pad curvature effect. The optimal bearing configuration with respect to

the maximum load capacity is found to be nearly independent on the journal eccentricity, pads number and compressibility number. The author concludes that Rayleigh step journal bearings have excellent load capacity and stable performance, albeit needing of a small number of pads at high compressibility numbers to have increased load capacity as compared to a plain journal bearing. Cunningham et al. [16, 17] investigate the rotor dynamic performance on herringbone grooved gas-lubricated journal bearings. The experiments show a good load capacity is achieved at groove-to-ridge ratios of 2.0 to 2.4. The effects of herringbone-groove geometries and clearance on half-frequency whirl are determined. The half-frequency whirl is very sensitive to radial clearance. A fully grooved bearing is more stable than a partially grooved one.

Galerkin weighted residual methods have been widely used in gas bearing analysis. Upwind FEM schemes have demonstrated efficiently in reducing pressure oscillations for operation at high bearing numbers [9, 18]. Faria and San Andrés [19] present an efficient numerical modeling for high-speed hydrodynamic gas bearings using finite element method with exact shape functions. The numerical procedures analyze diffusive–convective thin film gas flows in slider bearings and Rayleigh step bearings. A novel shape function is introduced to improve the computational efficiency and accuracy at high bearing numbers. In a Rayleigh step bearing, the pressure profile is invariant along the ridge and step regions at high bearing numbers. Predicted static stiffness are more accurate than the linearization analysis results by Hamrock [20]. Frequency-dependent dynamic force coefficients exhibit an increase in stiffness and a decrease in damping with respect to increasing frequency numbers.

Constantinescu [21] discusses the optimum bearing clearance for stabilizing gas bearing operation. Large clearances are evidently favorable for installation and render large operating eccentricities. However the increase in clearance deteriorates the bearing dynamic behavior with the appearance of rotordynamic instabilities. Instability also occurs with very small clearances. Later on, Constantinescu and Galetuse [22] analyze the pressure variation due to fluid inertia effects in Rayleigh step bearings. For a small Reynolds number (laminar flow) and small film thickness ratio before and after the step,

a pressure drop occurs as the flow entering the land is accelerated; otherwise a pressure rise will take place as the turbulence and large film thickness ratio decelerate the flow.

The grooves etched on the step bearing cause a pressure discontinuity along the bearing circumferential direction. Bonneau et al. [9] develop a two-dimensional FEM for grooved gas face seals. An integral equation is developed to avoid discontinuities in the film thickness. An upwind method introducing a nonsymmetrical weight function is efficient to solve Reynolds equation, providing satisfactory behavior even when the faces are misaligned. Foster et al. [23] apply an average clearance to discontinuous surfaces of a grooved bearing. The effect of varying groove numbers on the bearing stiffness is quite small. Zirekelback and San Andrés [24] investigate the performance of Herringbone grooved journal bearings using a finite elements analysis. A parametric study indicates that equal groove and land widths provide the best conditions for higher direct stiffness. The authors point out that when the grooved journal rotates at a fixed journal eccentricity, the film thickness is non-stationary since the local film thickness varies due to the grooves; thus the fluid film reaction forces and force coefficients vary periodically. This effect is pronounced for a low number of groove and large journal eccentricities. The bearings perform like a source of parametric excitation in a rotor/bearing system.

Fonda [25] details, theoretically and experimentally, the performance of Akers shaped Rayleigh step bearings with axial grooves. This type of bearing apparently exhibits large load capacity and dynamic stability, with small and nearly constant cross coupling stiffness coefficients. In addition, a near frictionless carbon (NFC) coating applied on the rotor surface reduces the friction and lift-off time for a test rotor. An effective friction coefficient on the order of 0.0005 is calculated from test measurements. Ajayi et al. [26] investigate the performance of amorphous carbon coating, namely NFC coating, in turbocompressor air bearings. The coatings evidently prevent the rotor wall climbing for smooth sliding contact during start-up and shutdown. Quick lifting of the rotor in the air bearings reduces the wear and damage of solid surfaces for long durability of the bearings under cyclic start/stop operation.

Sastri et al. [27] study the tribological properties of diamond like carbon (DLC) coatings and their compatibility with a wide range of substrates. The authors report that DLC coatings on air bearings show extremely high wear resistance, protecting the bearing surfaces when spinning with and without the presence of air. Dellacorte et al. [28] evaluate chrome oxide and chrome carbide coatings on journals in sliding contact against either bare superalloy or Al_2O_3 coated foil bearings. Extensive repeat start/stop cycles show rubbing of the journal surface against foil bearing at shaft speeds below 5,000 rpm. The wear characteristics of the bearings are greatly improved by applying a protective coating Al_2O_3 on the foils.

Two kinds of instabilities are apparent in hybrid gas bearings, i.e. pneumatic hammer and hydrodynamic instability. Pneumatic hammer is excited by the external pressurized gas and sustained when the journal velocity and pressure are out of phase. Stowell [29] investigates the effect of supply recess configuration and supply orifice size on the occurrence of pneumatic hammer in a gas-lubricated externally pressurized annular thrust bearing. Improper restrictor design with large volumes is prone to result in this dangerous instability that can occur even without rotor spinning. Hydrodynamic instability is characterized by the frequency equal to or less than half of the running speed due to the loss of damping capacity at high shaft speed. San Andrés and Childs [30] demonstrate that hybrid bearings with angled injection improve rotordynamic performance with virtual elimination of cross-coupled stiffness coefficients and null or negative whirl frequency ratios. Czolczynsk [31] provides a comprehensive review of gas bearing applications and the numerical analysis for prediction of frequency dependent force coefficients. San Andrés and Wilde [32] advance the finite element analysis of gas bearings using efficient high order weight functions. Numerical results are deemed accurate for arbitrary speed numbers. References [6], [7], [33] and [34] detail the research at TAMU on inexpensive gas bearings.

The present work advances the technology of gas film Rayleigh step bearings, for applications to oil-free turbomachinery by demonstrating their rotordynamic performance, reliability and durability.

EXPERIMENTAL FACILITY

Figure 1 shows the experimental high speed test apparatus and instrumentation for gas bearing investigations[1]. Wilde [34] developed the test rig and described its major features.

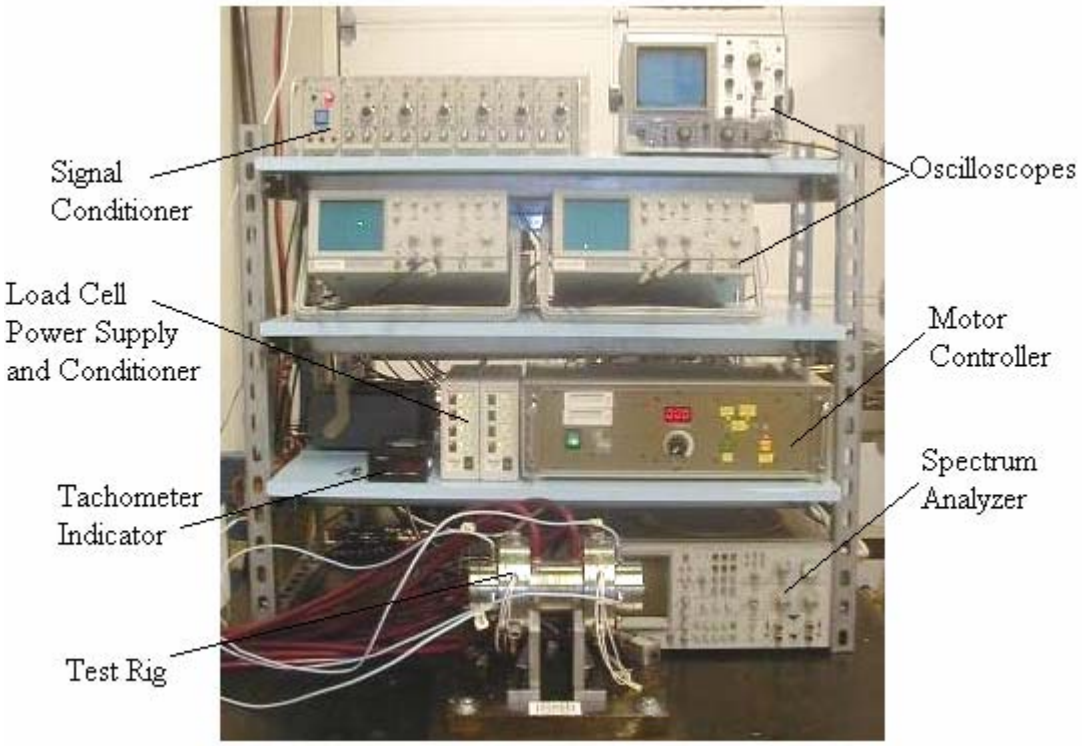

Fig. 1 Gas bearing test rig and instrumentation

Figure 2 depicts the test rig of a symmetric construction and with a steel main body integrating a brushless AC motor armature. The motor controller provides 0.9 kW of continuous power. The maximum continuous speed can approach 99,999 rpm. A K-type thermocouple attached to the motor inside the test chamber monitors the

[1] This test rig currently stands in the Turbomachinery Laboratory at Texas A&M University.

temperature of the motor armature. A rapid temperature rise is a good indicator of solid surface contact of the rotor with its bearings.

The motor drives a rotor supported by two identical gas film bearings. This rotor consists of a steel shaft, 15 mm diameter and 190 mm in length, onto which two cylindrical sleeves are tight fit. The rotor for the test Rayleigh step bearing has a maximum diameter of 29.000±0.002 mm with NFC (Near-Frictionless Carbon) coating. Eight 1 mm in diameter holes are spaced equally at each rotor end face. Small masses can be placed in these holes for adjusting rotor balancing and calibrated imbalance response measurements. Thrust pins and lock nuts in both casing covers prevent axial rotor movements.

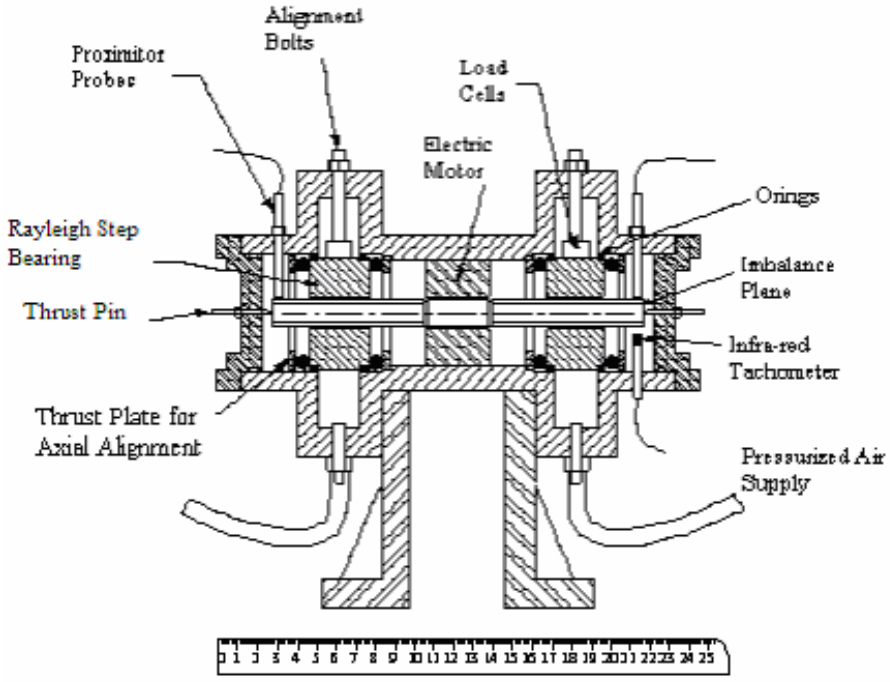

Fig. 2 Schematic cross section view of test rig (Unit: cm)

The bearings are installed into the test rig with load cells and positioned using three alignment bolts 120 ° apart. A cover plate pushes each bearing into the test rig, and O-rings on each bearing side seal the bearing chamber preventing air leakage. Alignment

plates and loose through bolts assist in the positioning of each bearing within its housing. The airflow into the bearing is controlled by on/off valves connected to the main pressure source (shop line). The gas piping system includes a pressure regulator, dryer/filter, and pressure gauges and flowmeters.

Figure 2 shows two orthogonally positioned eddy-current displacement sensors installed into each casing end to measure rotor motions. The outputs of these transducers are connected to a signal conditioner to remove the large DC bias offset and convert the signals within suitable ranges for the Labview® data acquisition system. Each oscilloscope displays the real-time, unfiltered shaft orbit at the rotor end side monitored. Unconditioned signals from the eddy-current transducers are connected to a Bently Nevada ADRE® data acquisition system. A two-channel dynamic signal analyzer displays the frequency components of selected signals in real time.

Three piezoelectric load cells, 120° apart, are mounted at the center plane of each bearing. These force sensors measure the load transmitted through the bearings. Three alignment bolts preload the load sensors and aid in the positioning of each bearing. An infrared tachometer, shown in Figure 2, installed inside one of the bearing chambers records the rotor speed and offers a keyphasor signal for data acquisition. Table 1 provides the sensitivities of the displacement and load sensors and the range of the flowmeters.

Table 1 Sensitivities and ranges of measurement sensors

Name	Location	Sensitivity	Unit
Force Transducer	Left Bearing	119	mV/N
	Right Bearing	120	mV/N
Displacement Proximity probe	Left Bearing	40	mV/μm
	Right Bearing	40	mV/μm
Flow Meter (range)	Left Bearing	100	L/min
	Right Bearing	50	L/min

The ADRE® data acquisition system acquires and saves the data during rotor coast-down response tests. The DAQ system has two channels for keyphasor signals and eight input channels for other signals. Four rotor displacement signals and a maximum of four load sensor signals can be collected simultaneously. The DAQ system also provides various outputs including Bode plots, cascade diagrams, orbit plots, spectrum diagrams, real time slow roll subtraction as well as synchronous response filtering. The maximum rotor speed for the DAQ system is 60,000 rpm. The Labview® DAQ system has eight input channels. Seven displacement / load signals can be collected at the same time with one channel reserved for the tachometer trigger signal. An ad-hoc Labview® Virtual Instrument program developed in the laboratory provides snapshot views, waterfalls, etc. This DAQ supplements others for high speed tests above 60,000 rpm.

Test Bearings and Rotor

Rayleigh step rotor / bearing

Figure 3 displays the assembly geometry of the test rotor. The rotor, weighing 0.87 kg, consists of a 4140 steel shaft with a diameter of 15 mm and 190 mm in length. The motor armature is located in the middle of the rotor assembly. Residual magnetism of the rotor is reduced to its lowest level possible to ensure even rotation, i.e., without intermittent starts/stops and high frequency chattering. Two cylindrical steel sleeves with NFC (Near-Frictionless Carbon) coating are fit onto the shaft. Elementary Akers shaped Rayleigh steps are etched by recessing the surface of the shaft below the original cylindrical surface. Figure 3 also shows two Akers shapes on the rotor surface. Four axial grooves separate the Rayleigh steps. The grooves are 3 mm wide and 2.2 mm deep.

Experiments were performed for two pairs[2] of cylindrical bearings and a rotor with Rayleigh-step journals. The two test bearing pairs have smooth 4140 steel cylindrical bores with nominal diameters of 29.050 mm and 29.076 mm, respectively. The counterpart of the rotor has a nominal diameter of 29 mm with NFC coating. Figure

[2] Another pair of bearings with a nominal sleeve diameter of 29.025 mm (nominal radial clearance of 10.25 μm) was difficult to install and align due to its tight clearance. The rotor was prone to stick to the bearings at low shaft speeds during the coastdown tests. No data was collected for this bearing pair.

4 displays the Rayleigh step bearing and rotor, and a detail view of step and groove characteristics on the rotor surface. Pressurized air enters the bearing through three radial identical orifices, 120° apart in the middle plane of the bearing. Table 2 details the geometry of the rotor and test bearings.

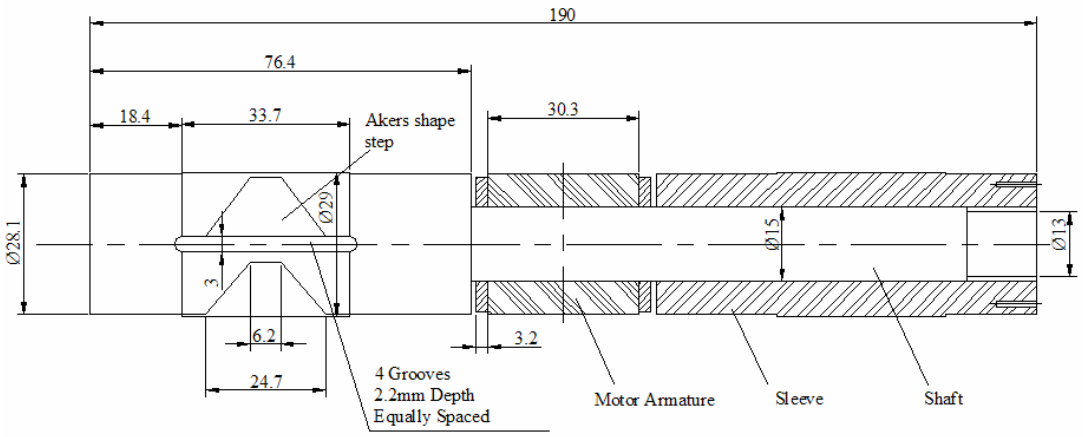

Fig. 3 Geometry of test rotor with shaft, motor armature and bearing sleeves (Units: mm)

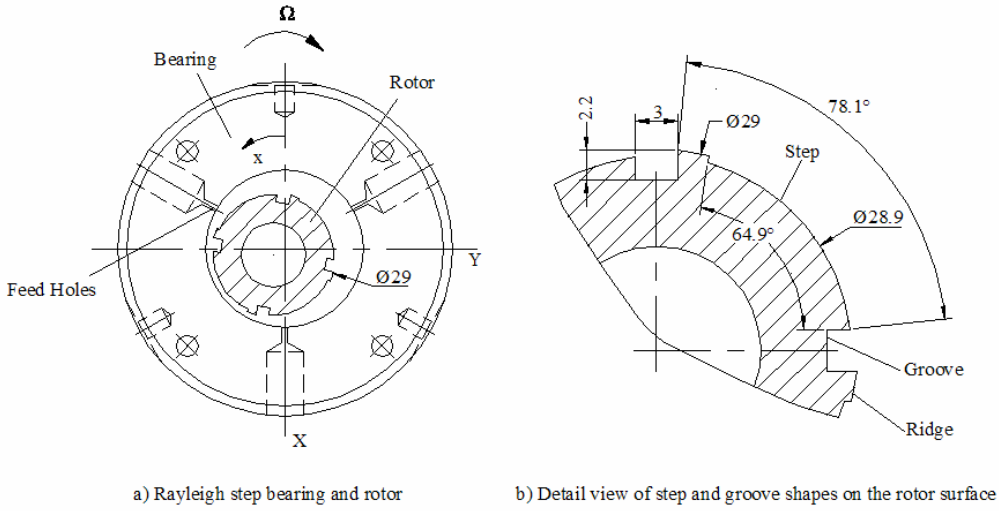

Fig. 4 Schematic view of test Rayleigh step bearing and rotor; and a detail view of steps and grooves on the rotor surface (Units: mm)

Table 2 Geometry of Rayleigh step bearings and rotor

Parameters	***Values***				***Units***
	Bearing set #1		Bearing set #2		
	B1	B2	B1	B2	
Measured bearing diameter, D_b (Original as delivered)	29.072 ±0.001	29.074 ±0.001	29.046 ±0.001	29.050 ±0.001	mm
Design diametrical clearance	76.2		50.8		μm
Bearing diametrical clearance, 2C (Original as delivered)	72±3	74±3	46±3	50±3	μm
Rotor diameter, D	29±0.002				mm
Rotor mass, M	0.87				kg
Rotor length, L	190				mm
Step diameter	28.90				mm
Step depth	50				μm
Step angle	64.9°				--
Step arc length	16.4				mm
Step number	4				--
Pad angle	78.1°				--

Free-free mode natural frequency of the test rotor

Rap tests facilitate the experimental determination of the rotor's 1st and 2nd free-free natural frequencies and corresponding mode shapes. Two piezoelectric accelerometers were wax-attached to the wire-suspended rotor in the test. One stationary accelerometer was fixed on one end of the rotor as a reference source. A roaming accelerometer moves axially along the rotor surface to capture responses at various axial locations when impacting the rotor with a hammer. A digital signal analyzer records the rotor responses excited by the hammer; then natural frequencies can be determined

where the peak responses occur. Associated response amplitudes and phases between two accelerometers determine the mode shapes at natural frequencies.

A physical model created with XLTRC^2 [35] predicts free-free natural frequencies of the test rotor. The rotor model is sectioned into 16 elements, as shown in Figure 5. Zero clearance fits are applied between sleeves and shaft in the modeling. Proper material properties are used respectively to each part of the assembly rotor. Grooves machined on the rotor surfaces are considered for the mass and inertia reduction in the modeling.

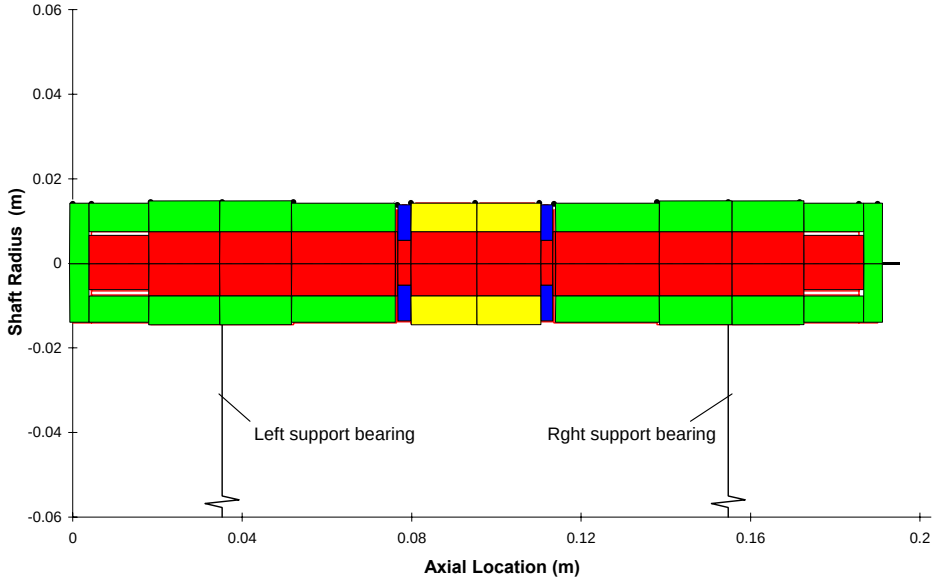

Fig. 5 Structural FE rotor model for rotordynamic response prediction

The free-free natural frequencies are inherent characteristics of the rotor in absence of the bearing supports. Table 3 lists the free-free natural frequencies obtained from measurements and evidencing good correlation with predictions from XLTRC^2, Note the natural frequencies are much higher than the maximum motor speed (99,999 rpm). Thus, the rotor in the test speed range (less than 30 krpm) is apparently rigid.

Figure 6 and Figure 7 show the elastic free-free mode shapes at each natural frequency from the rap tests and predictions from XLTRC^2. Predictions match well with

the experimental measurements. Note that maximum deflections occur at the end of the rotor for both bending modes. Deflections are small at the bearing nodes, as shown in the figures.

Table 3 Free-free natural frequencies of the test rotor

Free-free Natural Frequencies	Measurement (Hz)	Prediction (Hz)
1st bending mode	1,920	1,922
2nd bending mode	6,560	6,626

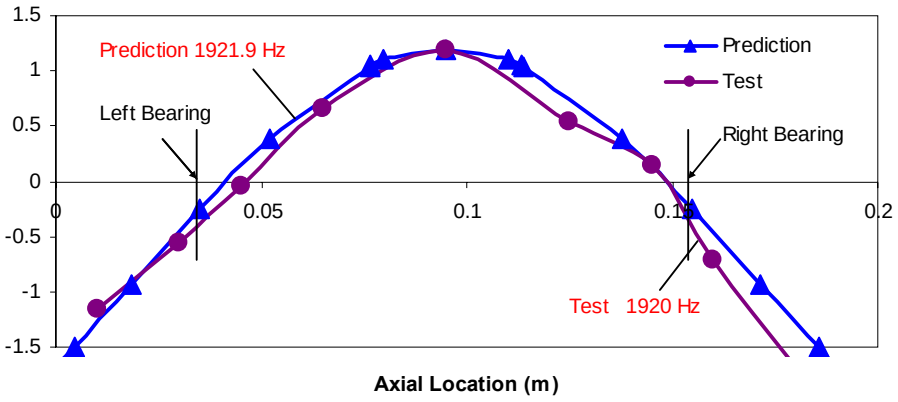

Fig. 6 Comparison of measured and predicted first free-free mode shape of the test rotor

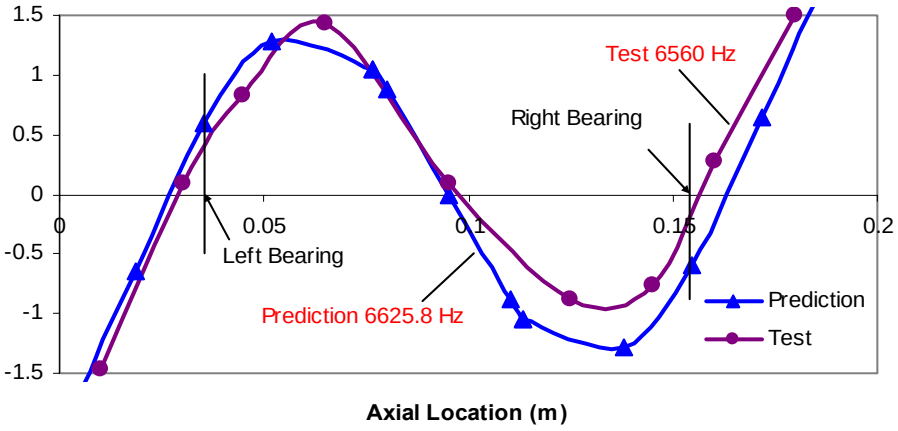

Fig. 7 Comparison of measured and predicted second free-free mode shapes of the test rotor

EXPERIMENTAL RESPONSE OF THE ROTOR SUPPORTED ON RAYLEIGH STEP BEARINGS

The dynamic performance of a rotor supported on Rayleigh step gas bearings is obtained from coast down tests for various gas supply pressures. The coastdown tests avoid the motor torque influence on the rotor dynamic performance. Coast down tests can provide meaningful characteristics of the rotor motions, consisting of passage through critical speeds, damping capability and speeds of instability (onset of sustainable subsynchronous whirl). The critical speed is determined at the shaft speed showing the peak response to imbalance with a 180° phase change. A good damping ability is indicated by acceptable vibration amplitude when traversing a critical speed. The rotor-bearing system stiffness determines the critical speed; which can be identified from the imbalance response. External feed air pressures have significant effects on the rotor performance, reducing the rotor friction during start-up[3] and shutdown; affecting the critical location and the stable operation speed range. The benefit of hybrid (combination of hydrostatic and hydrodynamic effects) operation on rotor performance is demonstrated for various supply gas pressures.

Chronology of the Tests Conducted with Rayleigh Step Bearings

The rotor coastdown tests started with bearing set #1 (38.1 μm nominal radial clearance). The NFC coating on the rotor surface was intact at the beginning of the tests. In the repeated rotor start/stop experiments, the coating was gradually damaged due to the rotor/bearing contact at low shaft speeds. Hence, the rotor diameter was reduced and bearing clearances were enlarged.

Then, coastdown tests were conducted with bearing set #2 (25.4 μm nominal radial clearance). The NFC coating was further removed from the rotor surface during these tests. Post inspections after completion of all tests showed the NFC coating on the rotor surface was completely removed due to sustained wear of the solid surfaces; first

[3] The rotor can spin even without external pressurized air.

as a result of intermittent contact, and then continuous hard rubbing at low shaft speeds where the gas bearings could not support the rotor. Table 4 gives the test timeline for the Rayleigh step bearings and measured bearing clearances during the tests. Note after the completion of all tests, the clearance of bearing set #2 was increased by ~7 μm. Severe rubbing and hard contact at low shaft speeds not only destroyed the NFC coating but also removed metal from the steel shaft and bearings surfaces.

Table 4 Test timeline of Rayleigh step bearings and measured bearing clearances.

Test timeline		Measured Bearing Radial Clearance (μm)			
		Bearing set #1		Bearing set #2	
		B1	B2	B1	B2
Measurement prior to any testing, NFC coating[4] on the rotor surface is intact		36 ± 3	37 ± 3	23 ± 3	25 ± 3
Conducted tests with bearing set #1. NFC coating on rotor was partly damaged after testing	Before tests	36 ± 3	37 ± 3		
	After tests	39 ± 3	39.45 ± 3	26 ± 3	28 ± 3
Conducted tests with bearing set #2. NFC coating on the rotor was gone after testing and shaft metal was partly removed	Before tests	N/A		26 ± 3	28 ± 3
	After tests	N/A		30 ± 3	31.25 ± 3

Rotor Imbalance Response with Coast-down Tests on Rayleigh Step Bearings

Coast-down tests to record remnant imbalance response of the rotor supported on Rayleigh step bearings were conducted at three absolute supply pressures, 2.39, 3.77 and 5.15 bar (20, 40, 60 psig), respectively. The two test bearing sets have nominal radial

[4] The nominal coating thickness is unknown. The manufacturer (Meruit, Inc.) did not measure the coating thickness of this rotor as the thickness is less than the tolerance for the manufacture of the rotor parts. Argonne National Laboratory deposited the NFC coating on the rotor, typically with a ~2 μm thickness.

clearances of 38.1 μm and 25.4 μm[5], respectively. The effects of bearing clearance on the rotor performance are determined from the coast down imbalance responses. The rotor coastdown tests started below the threshold speed where sustained large subsynchronous vibrations set in. Data acquisition systems (DAQ) collect the rotor displacements and bearing transmitted loads. Proper configurations of the DAQ system for ADRE® and Labview® ensure the accuracy of the recorded data, facilitating the post-process of the experimental results.

Coastdown rotor responses with test bearing set #1[6]

Figure 8 shows a waterfall plot depicting the rotor displacement response versus frequency for an absolute supply pressure at 2.39 bars (20 psig). The shaft speed ranges from ~ 2 krpm to 20 krpm. Above this top speed, large amplitude sustained subsynchronous whirl motions were excited. Data represents the measurement at the left bearing, vertical plane. Dominant synchronous and low level amplitude super-synchronous contents are evident for the rotor response. The rotor synchronous displacement responses approach peak amplitudes around 6,000 rpm, where a critical speed is traversed. The displacement amplitudes reach the lowest amplitude at 12 krpm then rise with the shaft speed. The rotor motion consists of broad band frequency components at low speeds, evidencing rotor rubbing or wall climbing. Rubbing happens as the gas bearings can not provide sufficient load capacity to fully support the rotor at low shaft speeds. Rotor motions are stable except that a transient subsynchronous vibration arises at the rotor speed of 13 krpm then fades away traversing this speed. The whirl frequency is nearly half of the synchronous frequency and coincident with the system natural frequency of 120 ± 4 Hz.

The waterfall plot in Figure 9 presents the frequency components of the rotor displacement responses for a test pressure at 3.77 bar (40 psig). Rotor responses are collected in the left bearing, vertical plane. The synchronous displacement amplitudes

[5] Actual bearing clearances are enlarged due to rotor coating wear, see Table 4.

[6] For bearing set #1, experiments were not conducted without external air pressurization.

decrease from the top speed of 20 krpm and increase approaching the critical speed region between 6 krpm to 7 krpm. The rotor operation is stable without any subsynchronous vibration. Harmonic components of the synchronous frequency have the small level amplitudes in the frequency domain. Dry friction due to rotor rubbing starts at low shaft speeds (~ 3 krpm) with broad band frequency components, as shown in the figure.

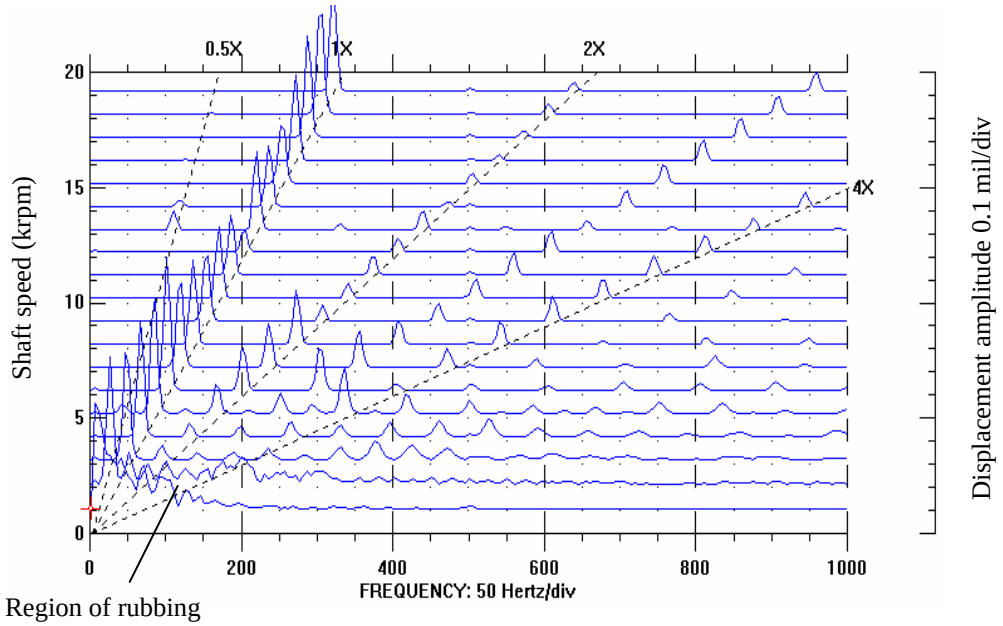

Fig. 8 Waterfall plot of rotor displacement amplitudes for a test pressure 2.39 bar (20 psig) at the left bearing, vertical plane. Test bearing set #1

Figure 10 shows the waterfall plot of the rotor coastdown displacement responses for an absolute supply pressure of 5.15 bar (60 psig). The displacement transducer is located at the left bearing, vertical plane. The rotor synchronous response amplitudes increase around a critical speed region at ~ 7,000 rpm. The displacements at the critical speed region show the largest magnitudes compared to the rotor responses at lower gas supply pressures of 2.39 bar and 3.77 bar, shown in Figures 8 and 9, respectively. Note a transient 0.5X subsynchronous component occurs at the rotor speed of 14 krpm. The

amplitude of this subsynchronous whirl is larger than the synchronous response. The transient subsynchronous whirl has a frequency close to the system natural frequency of ~ 124 Hz (7,440 rpm). Transient rubbing or uneven external gas supply may have caused the bounded subsynchronous whirls, shown in Figures 8 and 10. Supply gas pressures affect the amplitude and onset frequency of the subsynchronous whirl. The onset whirl frequency increases for a larger gas supply pressure at 5.15 bar. No subsynchronous vibration arises for gas supply pressure at 3.77 bar below 20 krpm.

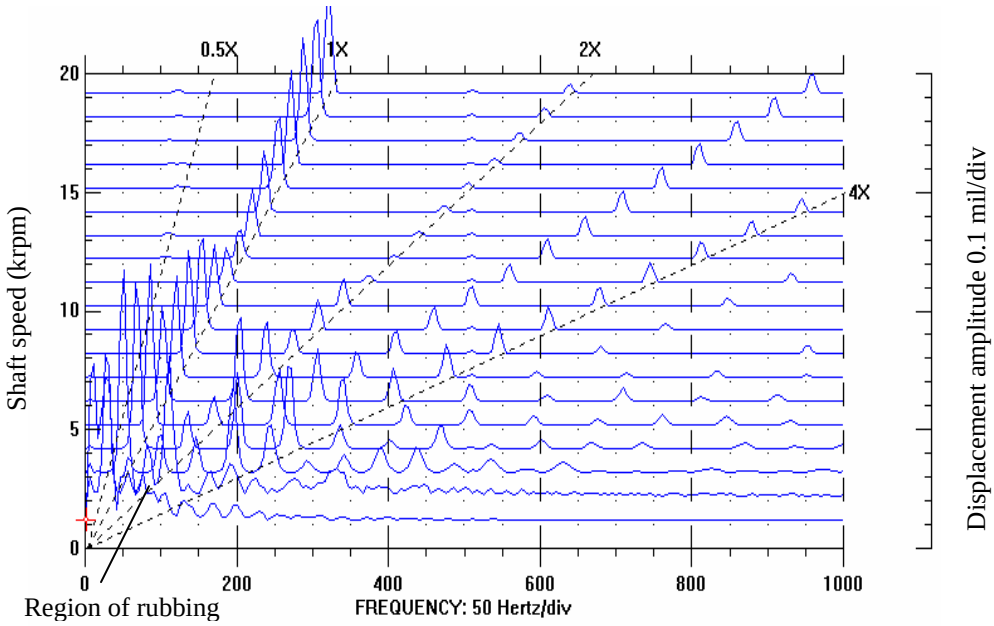

Fig. 9 Waterfall plot of rotor displacement amplitudes for a test pressure 3.77 bar (40 psig) at the left bearing, vertical plane. Test bearing set #1

Figures 8 through Figure 10 show the effect of gas supply pressure on the rotor dynamic performance of the test system. Increasing supply pressure provides more stiffness to the rotor-bearing system, increasing its critical speed from 6,000 to 7,000 rpm for supply pressures of 2.39 bar, 3.77 bar and 5.15 bar, respectively. Incidentally, the larger shaft amplitudes at the critical speed region evidence less damping derived for a higher supply pressure. This trend nearly holds for the other planes, i.e., hydrostatic pressurization increases the gas bearing direct stiffness and reduces the system damping

ratio while traversing a critical speed. References [6] and [7] report similar rotordynamic performance for other types of gas bearings.

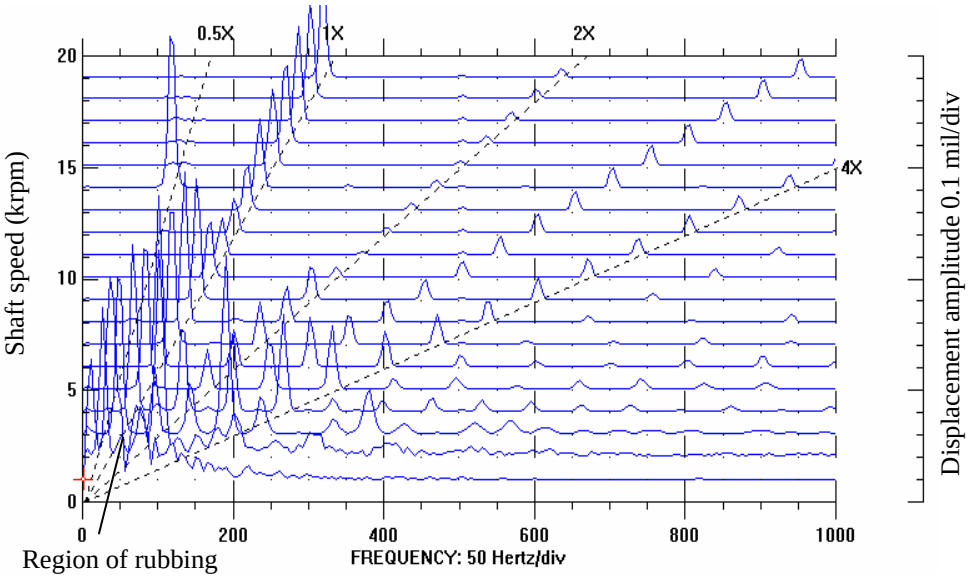

Fig. 10 Waterfall plot of rotor displacement amplitudes for a test pressure 5.15 bar (60 psig) at the left bearing, vertical plane. Test bearing set #1

Figure 11 depicts a waterfall plot of the bearing transmitted loads for gas supply pressure of 2.39 bar absolute (20 psig). The data correspond to transmitted loads at the left bearing, vertical plane. The synchronous transmitted loads reach a peak response at 13 krpm. Amplitudes of the synchronous transmitted loads are small around the critical speed region (6,000 rpm). At low shaft speeds, the transmitted loads consist of multiple frequency components (broad band frequency spectrum) where rubbing occurs as also seen in the displacement responses depicted in Figure 8.

Figure 12 shows the frequency components of the bearing transmitted loads for a test pressure of 3.77 bar (40 psig). Measurements are collected at the left bearing, vertical plane. The synchronous transmitted loads approach the highest level at a shaft speed of 11 krpm, while showing small amplitudes in the critical speed region of 6-7 krpm. Figure 13 depicts the bearing transmitted load amplitudes for a test pressure of

5.15 bar (60 psig). A half whirl subsynchronous reaction load appears at the shaft speed of 14 krpm where an associated transient subsynchronous whirl arises, as shown in Figure 10. The synchronous transmitted loads display peak magnitudes around the shaft speed of 10 krpm, showing low level amplitudes at the critical speed region around 7 krpm. Figures 11 through 13 demonstrate that at a higher gas supply pressure, the synchronous bearing transmitted load has smaller peak amplitude at a lower shaft speed, from 13 krpm, 11 krpm, to 10 krpm for test pressures of 2.39 bar, 3.77 bar and 5.15 bar. These speeds probably indicate the 2nd critical speed of the rotor bearing system. The Bode plot in Figure 14 shows clearly the load peak responses at these 2nd critical speeds for three supply gas pressures.

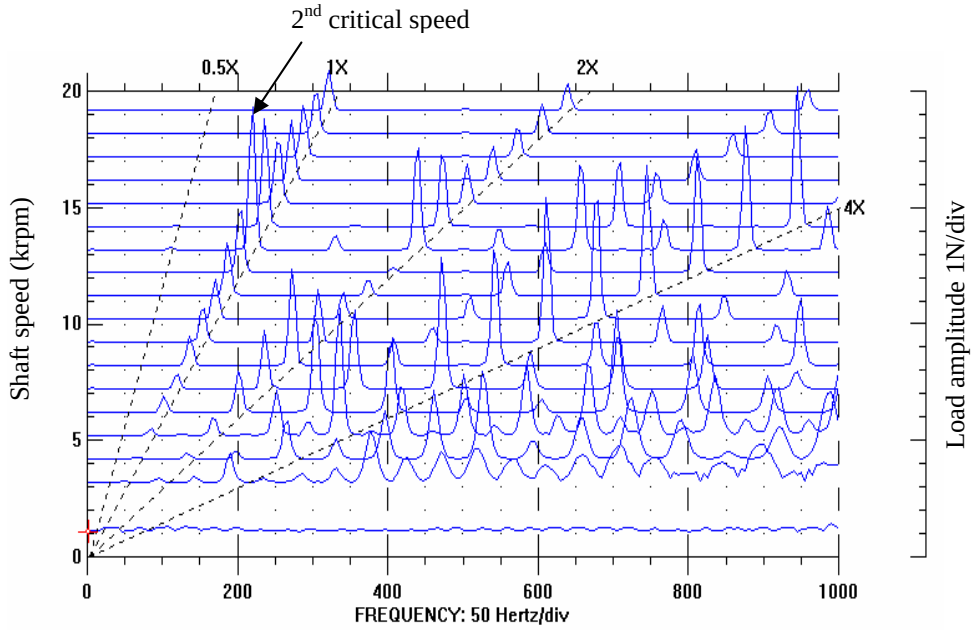

Fig. 11 Waterfall plot of transmitted load (left bearing, vertical plane) amplitudes for test pressures equal to 2.39 bar (20 psig). Test bearing set #1

Figures 11 through 13 depicting the transmitted load evidence a 4th order supersynchronous frequency with large level amplitudes, even higher than the synchronous magnitudes. The 4X components maintain large levels over the entire speed range, depending slightly on the running speed. Note the synchronous displacement

responses are dominant, as shown in Figures 8 to 10, while the magnitudes of 4th order displacement response are insignificant. Since the bearing transmitted load is proportional to the power two of frequency, even a small 4X displacement amplitude produces a large reaction force. On the other hand, the geometry of the Rayleigh step rotor, with four axial grooves separating steps and ridges, generates a time varying gas film and pressure field. The cyclic variations of the gas film, as the grooves are etched on the rotor surface, make the bearing perform like a source of parametric excitation in the rotor-bearing system [36]. The rotating pressure field results in an excitation which develops periodically depending on the number of grooves, delivering a large 4X super synchronous reaction load. In addition, when the rotor is in operation, each groove passes a feed orifice where the pressurized air enters into the bearing, enlarging the pressure difference between land/step and grooves (with ambient pressure). Figures 11 through 13 indicate that increasing gas supply pressure increases the amplitudes of 4th order bearing transmitted loads. Hence the geometry of the test bearings contributes to the 4X supersynchronous vibrations, with increasing supply pressures generating larger reaction loads.

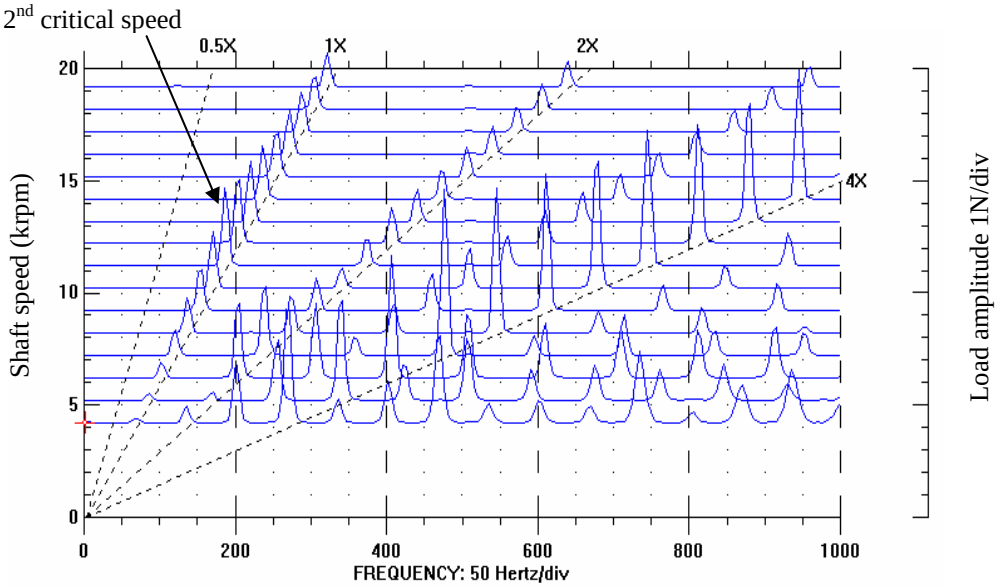

Fig. 12 Waterfall plot of transmitted load (left bearing, vertical plane) amplitudes for test pressures equal to 3.77 bar (40 psig). Test bearing set #1

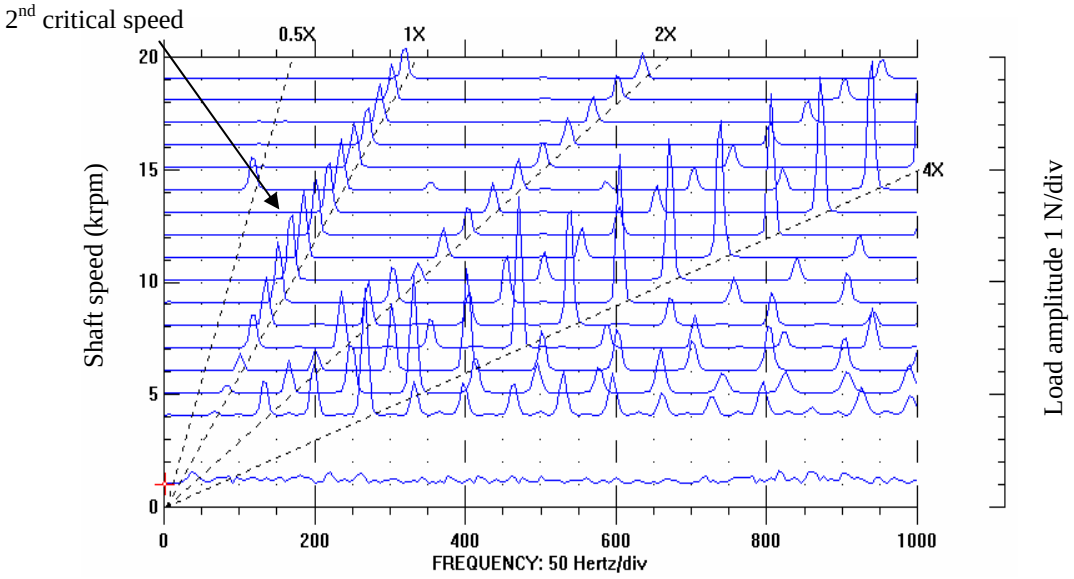

Fig. 13 Waterfall plot of transmitted load (left bearing, vertical plane) amplitudes for test pressures equal to 5.15 bar (60 psig). Test bearing set #1

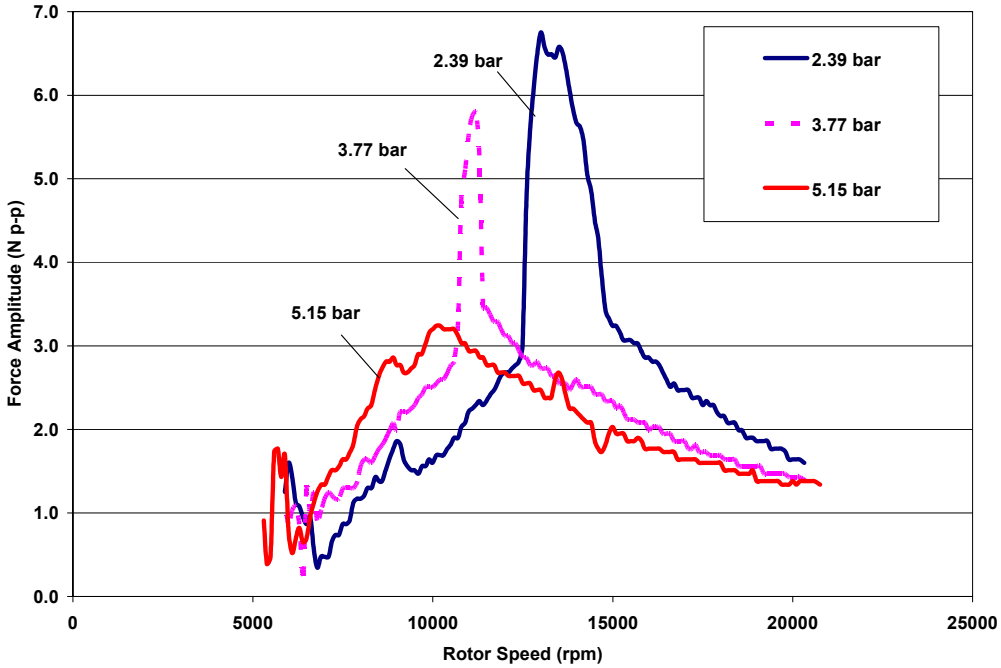

Fig. 14 Synchronous components of transmitted loads versus rotor speed for three test pressures of 2.39, 3.77 and 5.15 bars. Measurements recorded on test bearing set #1, left vertical plane.

For test bearing set #1, Figure 15 shows a typical rotor coastdown speed versus time for a supply pressure at 2.39 bar (20 psig). The speed decreases almost linearly with time when the rotor coasts down from 20 krpm to ~5 krpm. In this speed region, the rotor is operating on a gas film. Below 4 krpm, the rotor speed drops quickly as severe dry friction (rubbing) occurs, as shown also in Figure 8. Rubbing contact of the rotor against its bearings damaged the applied NFC (Near-Frictionless Carbon) coating on the rotor surface. Appendix A shows more coastdown speeds for other test conditions, including comparison to the performance of flexure pivot–tilting pad gas bearings.

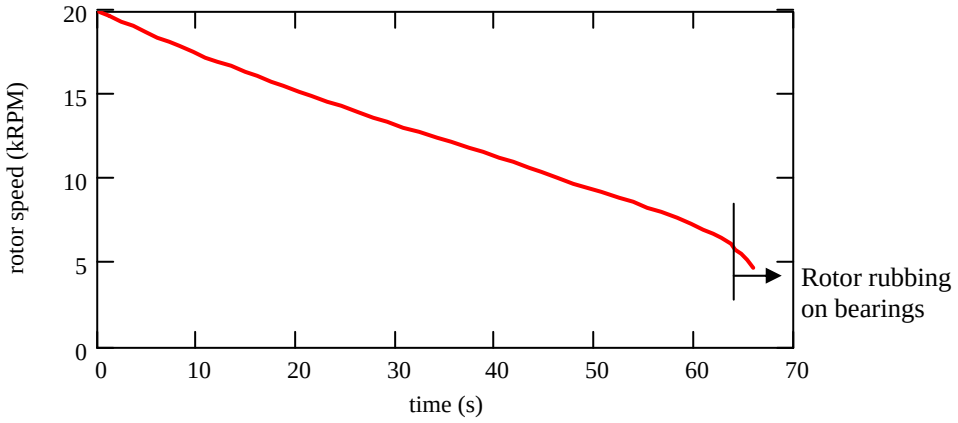

Fig. 15 Typical rotor coastdown speed versus time for test bearing set #1 with supply gas pressure of 2.39 bar

Figure 16 shows typical time traces of rotor displacements, vertical and horizontal, at speeds of 12.4 krpm, 13.1 krpm and 14.3 krpm for a supply pressure of 2.39 bar. Figure 16 (a) depicts the rotor motions at the left bearing side at a speed of 12.4 krpm. Since the horizontal displacement transducer is located ahead of the vertical one in terms of the rotational direction, the peak response advances at the horizontal plane demonstrating a forward whirl motion. At the rotor speeds of 12.4 krpm and 14.3 krpm, shown in Figures 16 (b) and 16 (d), vertical rotor motions at the right end are evidently 180° out of phase from the left end, indicating conical mode motions. At 13.1 krpm,

Figure 16 (c), rotor displacements at each end display the same phase demonstrating a dominant cylindrical mode. The phase shift possibly results from the 2nd critical speed (measured) around 13.1 krpm at the rotor vertical plane.

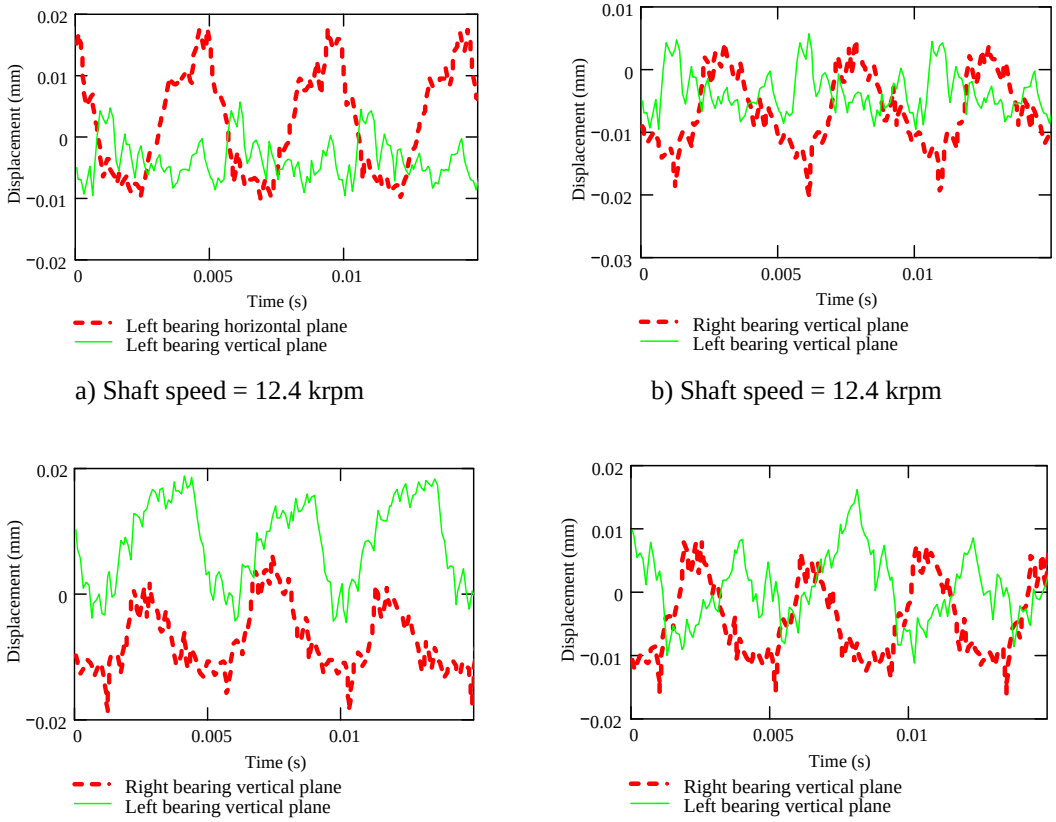

a) Shaft speed = 12.4 krpm

b) Shaft speed = 12.4 krpm

c) Shaft speed = 13.1 krpm

d) Shaft speed = 14.3 krpm

Fig. 16 Time traces of rotor motion at various shaft speeds. Absolute supply pressure of 2.39 bar; Test bearing set #1

Incidentally, Figure 14 also depicts an associated large synchronous transmitted load at this 2nd critical speed of 13 krpm for an absolute test pressure of 2.39 bar. Note the half frequency subsynchronous whirl is excited at this speed shown in Figure 8 and the whirl frequency is close to the rotor-bearing system natural frequency of ~120 Hz. The bearing transmitted loads exhibit the harmonics of 0.5X subsynchronous transmitted loads around the shaft speed of 13 krpm. Similarly, the rotor-bearing system show the

2^{nd} critical speeds at ~11 krpm and ~10 krpm for the test pressure of 3.77 bar and 5.15 bar, respectively, as shown in Figure 14. Increasing gas supply pressures reduce the 2^{nd} critical speeds while increasing the damping capability.

Figure 17 shows the static displacement of the rotor centerline with respect to rotor speeds for a test supply pressure of 2.39 bar. The rotor DC offset, averaged from time trace values, represents the relative position between rotor centerline and geometric center of the bearing. At the vertical planes, the rotor centerline has a falling trend from the bearing center during the coastdown tests for both bearings, shown in Figure 17 (a) and 17 (c). The increasing eccentricity with declining rotor speed indicates a smaller film thickness required for carrying the rotor weight at low speeds. The DC offset at the left bearing has a jump between speeds of 12-14 krpm as shown in Figure 17 (a), where large bearing reaction loads occur at the left vertical plane, as noted also in Figure 14 for test pressure 2.39 bar. Offset magnitudes along the horizontal plane are small in Figure 17 (b) and 17 (d), and show opposite directions for each bearing versus rotor speeds. Figure 17 (e) depicts the loci of the shaft center versus rotor speed at both bearing locations. A large positive magnitude at the left bearing vertical direction appears at a speed around 13 krpm.

Figure 18 shows the rotor overall peak-peak amplitudes of bearing transmitted loads for a supply pressure of 5.15 bar (60 psig). The notations in the Bode plot indicate the force transducer locations; namely, L_V for left bearing vertical direction; L_120CCW and L_120CW for the left bearing load sensors positioned 120 degree away from the vertical plane, counter and clockwise, respectively. The overall transmitted load amplitudes vary little at high rotor speeds; increase to 35 N as the rotor approaches the lowest critical speed region about 7,000 rpm, and maintain this high level even at lower shaft speeds. The waterfall plot in Figure 13 indicates the synchronous transmitted load has the low level amplitudes in the speed region from 5 krpm to 20 krpm. The transmitted loads at low shaft speeds increase as severe rubbing occur, as also seen in Figure 10.

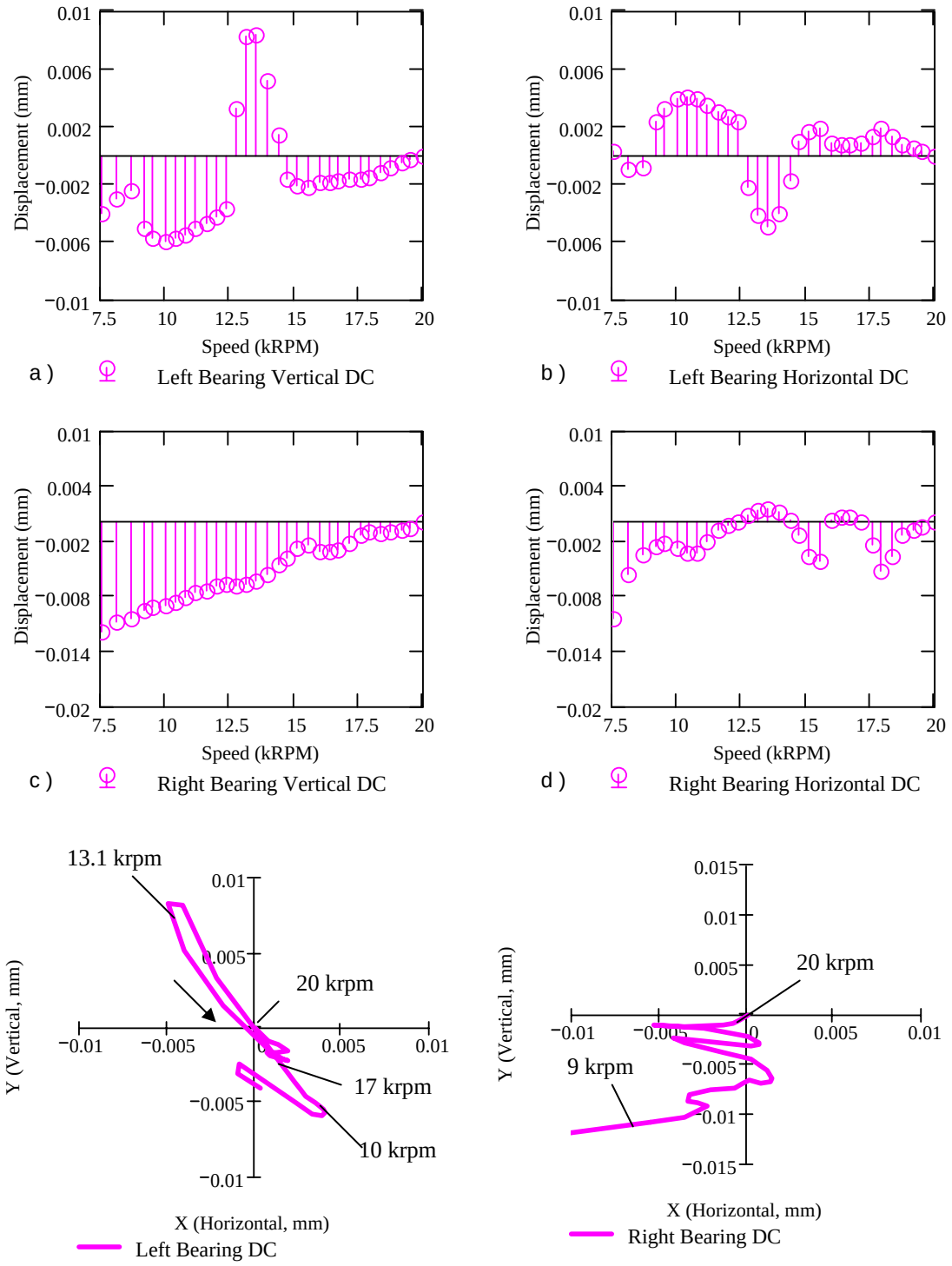

e) DC offset traces for both bearings

Fig. 17 Shaft center static motions in vertical and horizontal planes for a test pressure 2.39 bar. Test bearing set #1

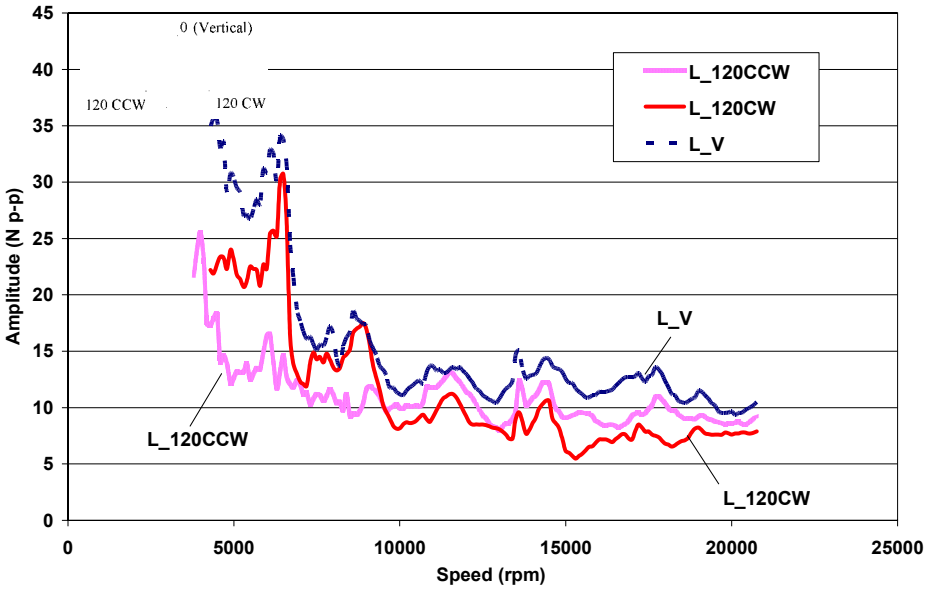

Fig. 18 Overall components of bearing transmitted load peak-peak amplitudes at supply gas pressure of 5.15 bars. Test bearing set #1. L_V-Left bearing vertical plane, L_120CCW-Left bearing 120 counterclockwise from the vertical plane, L_120CW- Left bearing 120 clockwise from the vertical plane.

Coastdown responses with test bearing set #2[7]

Baseline imbalance responses

Figure 19 shows the waterfall plot for the rotor displacement and bearing transmitted load responses at a test pressure of 3.77 bar. The data correspond to the right bearing, vertical plane. The critical speed is identified around 8,000 rpm. A high level (0.5X) subsynchronous response is evident at 14,500 rpm. This subsynchronous whirl was sustainable when the rotor speed was increased. The rotor motion shows stable response below the highest speed of 14,500 rpm, free from subsynchronous whirl during the coastdown. The synchronous displacement responses are dominant with small supersynchronous components for most speeds. At low speeds, the rotor motions consist of broad band frequency components evidencing rubbing against the bearings.

[7] The actual bearing radial clearance was enlarged to 31.25 μm due to wear of rotor coating and metal removal from the solid surfaces.

Transmitted synchronous bearing loads are small at the critical speed region around 8,000 rpm. The (4X) supersynchronous components are insignificant in the displacement response while bearing transmitted loads present considerable 4X supersynchronous amplitudes, i.e., similar to the rotor coastdown responses shown earlier on the test bearing set #1 (Figure 9 and Figure 12).

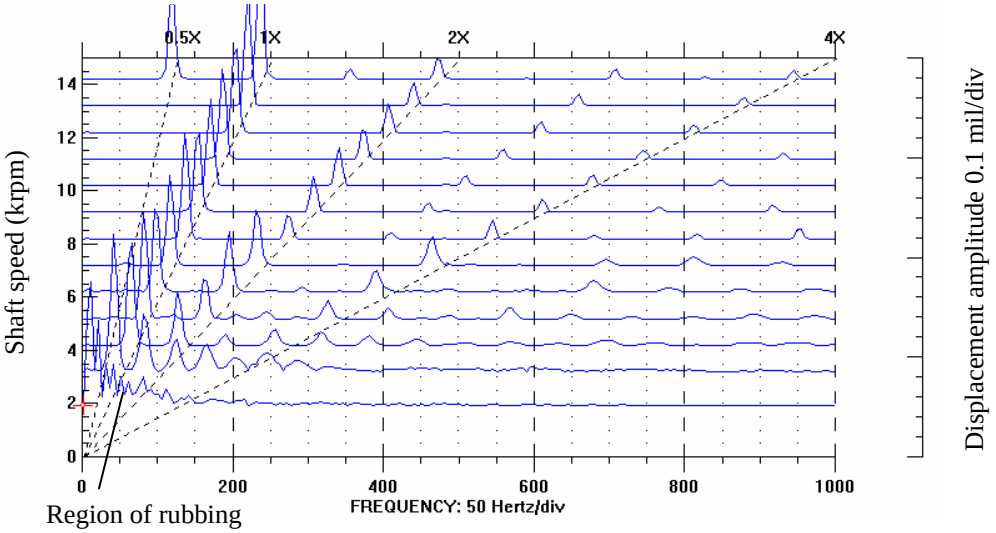

a) Displacement response

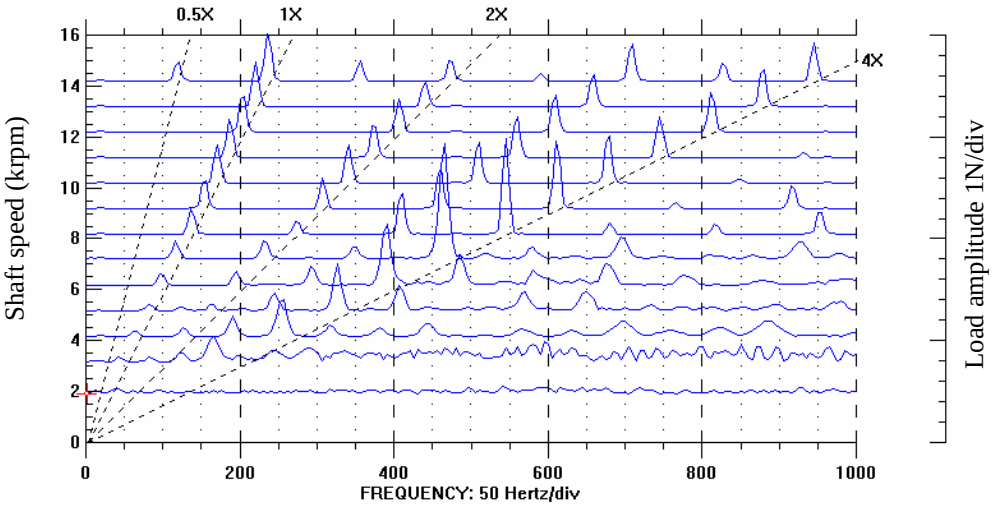

b) Bearing transmitted load

Fig. 19 Waterfall plot of rotor displacement and bearing transmitted load amplitudes for the test pressure of 3.77 bar (40 psig) at right bearing vertical plane. Test bearing set #2

Investigations of the rotor performance without supply gas pressure were conducted with a low gas feed pressure (2.39 bar) at startup to reduce rubbing of the test rotor. The rotor was brought up to a speed of ~ 10 krpm, and then the supply pressure was shut off. Immediately after, the rotor was accelerated to a higher speed, ~ 15 krpm, and below the onset speed of instability. Figure 20 shows a waterfall plot of the rotor coastdown displacement response without gas supply pressure. The measurements were collected for test bearing set #2 at the left vertical plane. The rotor motion exhibits incipient rubbing at the highest shaft speed of 15,000 rpm where small amplitude motions appear with a broad band subsynchronous frequency. Probably, rubbing resulted in an uneven gas supply to the rotor, and then a temporary 0.5X subsynchronous vibration is excited, remaining from shaft speeds 14 krpm to 11 krpm in the coast down. After this event, the rotor operates well and decelerates quickly.

The rotor displacement responses are mainly synchronous in the speed region of 4 krpm to 14 krpm, with low levels of supersynchronous components. Below 4 krpm, the rotor speed drops quite quickly due to severe rubbing. The DAQ system did not work properly as the shaft deceleration was too quick for the DAQ configuration. In addition, the tachometer signal gave random values at very low shaft speeds (below 2 krpm). Figure 21 depicts the bearing transmitted loads at the left bearing vertical plane for the condition of no gas supply pressure. Note the 4X supersynchronous components maintain large amplitudes over the test speed, comparable with the synchronous components. This result confirms the Rayleigh step bearing geometry, rather than the gas supply pressure, determines the large 4X supersynchronous load responses. From the coastdown test without supply gas pressures, the Rayleigh step bearings exhibit an adequate load carrying capability; only at speeds above 4 krpm, however.

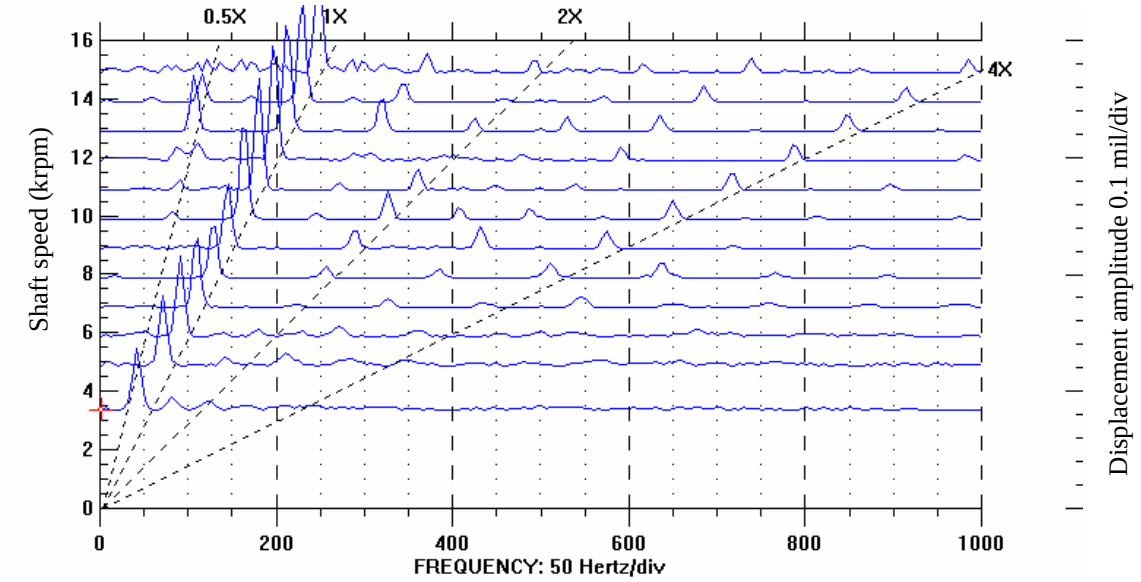

Fig. 20 Waterfall plot of rotor displacement amplitudes without supply gas pressure at left bearing vertical plane. Test bearing set #2

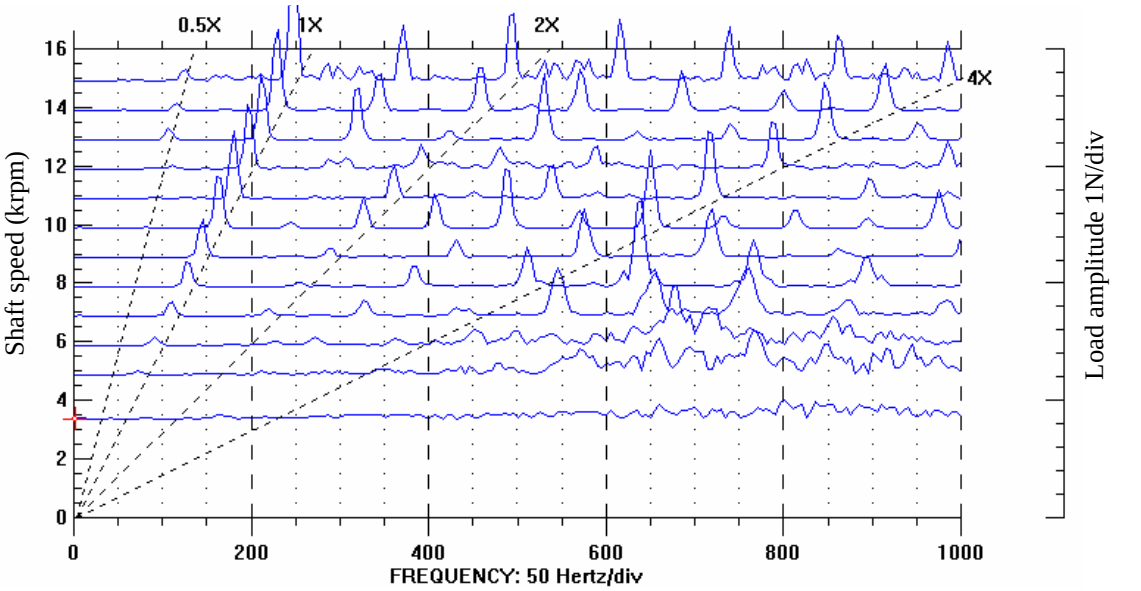

Fig. 21 Waterfall plot of bearing transmitted loads without supply gas pressure at left bearing vertical plane. Test bearing set #2

Figure 22 and Figure 23 display the rotor synchronous peak-peak amplitudes of displacement and bearing transmitted loads for test supply pressures of 1.01, 2.39, 3.77 and 5.15 bar (0, 20, 40 and 60 psig) at the left bearing vertical plane, without slow roll compensation. The rotor displacement amplitudes around the critical speed region (7,000-8,000 rpm) increase with increasing supply pressures, evidencing a declining damping capability. Critical speeds increase with the supply pressures, from 5,970 rpm, 7,090 rpm and 7,290 rpm to 7,690 for absolute supply pressures of 1.01, 2.39, 3.77 and 5.15 bar (0, 20,40 and 60 psig), respectively. The synchronous transmitted bearing loads, shown in Figure 23, exhibit peaks around the critical speeds for higher supply pressures at 3.77 bar and 5.15 bar. At low feed pressures of 1.01 bar and 2.39 bar, the transmitted bearing loads increase with shaft speed, no peaks arising at the critical speed region, ~7000 rpm. The synchronous components of the transmitted loads are small, less than 6 N over the test speed range for all feed pressures.

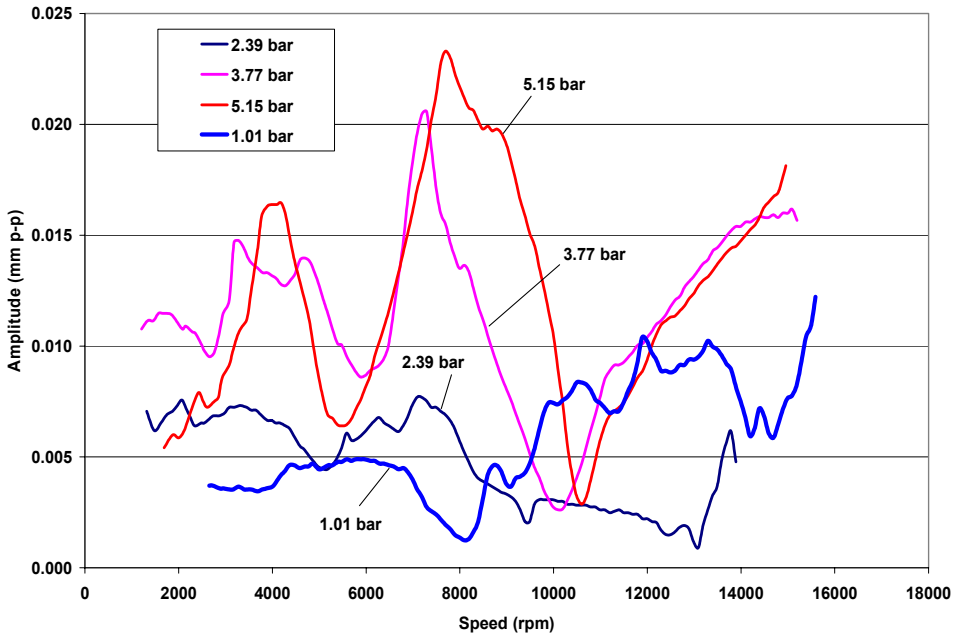

Fig. 22 Synchronous rotor displacement peak-peak amplitudes for various supply pressures, recorded at left bearing, vertical plane (without slow roll compensation). Test bearing set #2

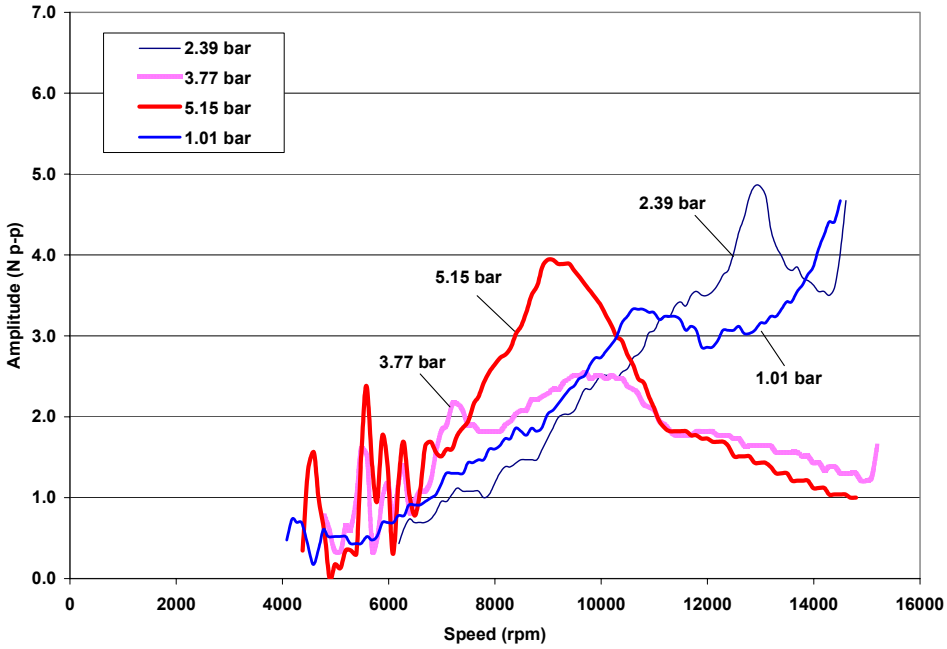

Fig. 23 Synchronous bearing transmitted load peak-peak amplitudes versus speeds for various supply pressures at the left bearing vertical plane. Test bearing set #2

Response of rotor to a calibrated imbalance

Calibrated imbalance rotor responses were obtained with added masses inserted at the rotor ends. A mass *(m)* of 0.042 gram was placed in the holes at the rotor ends at a radial location (*R'*) of 12 mm. The imbalance displacement (*u*), i.e. distance from rotor center of mass, is

$$u = \frac{mR'}{m + M_1} \qquad (1)$$

where M_1 is half the rotor mass (0.435 kg). Table 5 summarizes the imbalance conditions. Cylindrical and conical mode imbalance configurations were used for the tests as shown in Figure 24.

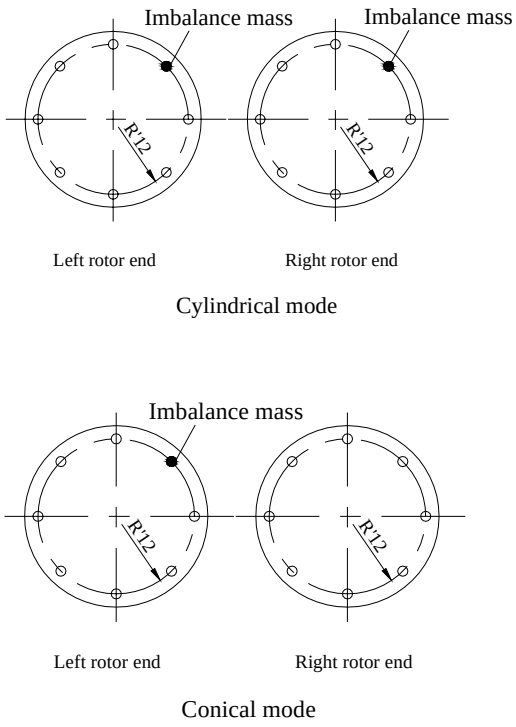

Fig. 24 Imbalance mass locations at rotor ends for cylindrical and conical mode excitation

Table 5 Calibrated imbalance conditions with conical and cylindrical mode excitations

Imbalance Name	Displacement *u* (μm)	
	Left rotor end	Right rotor end
U1 (conical mode)	1.16 ± 0.02	0
U2 (cylindrical mode)	1.16 ± 0.02	1.16 ± 0.02

Calibrated imbalance responses were obtained (without hydrostatic feed pressure) for test bearing set #2. Figure 25 shows the Bode plot of the rotor synchronous displacement peak-peak amplitudes for the baseline and calibrated imbalances. The data shown correspond to the left bearing horizontal plane and without slow roll compensation. As severe rubbing happens at low rotor speeds, the slow roll vector is

nearly impossible to identify at low speeds. Critical speeds at 7,000 rpm are apparent from the calibrated imbalance responses. The cylindrical mode imbalance excitation (U_2) determines a larger response at the critical speed than the conical mode (U_1). Figure 26 shows the peak-peak amplitudes of synchronous bearing transmitted loads recorded at the left bearing plane, 120° clockwise to the vertical direction. The cylindrical mode excitation (U_2) also determines a larger transmitted load at the critical speed. In addition, note the displacement amplitudes of baseline and conical mode imbalance responses are similar at the critical speeds, while the associated bearing transmitted loads show a large difference. The bearing transmitted load is not proportional to the displacement. The rotor motion exhibits a nonlinear behavior.

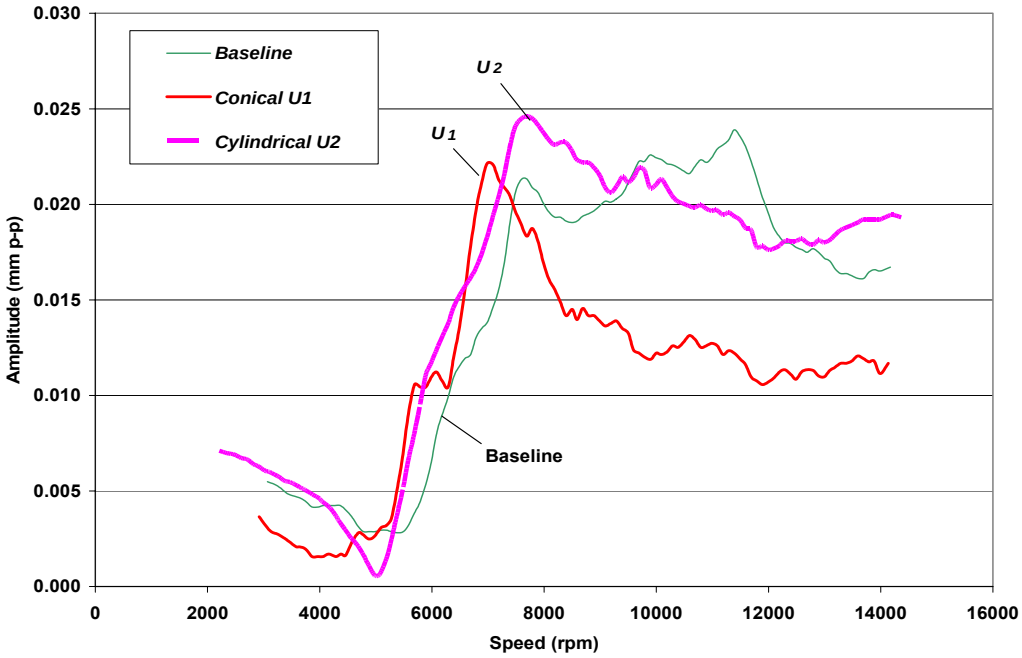

Fig. 25 Synchronous displacement peak-peak amplitudes for the rotor baseline and calibrated imbalance response, recorded at the left bearing horizontal plane, without slow roll compensation. No external supply gas pressure. Test bearing set #2

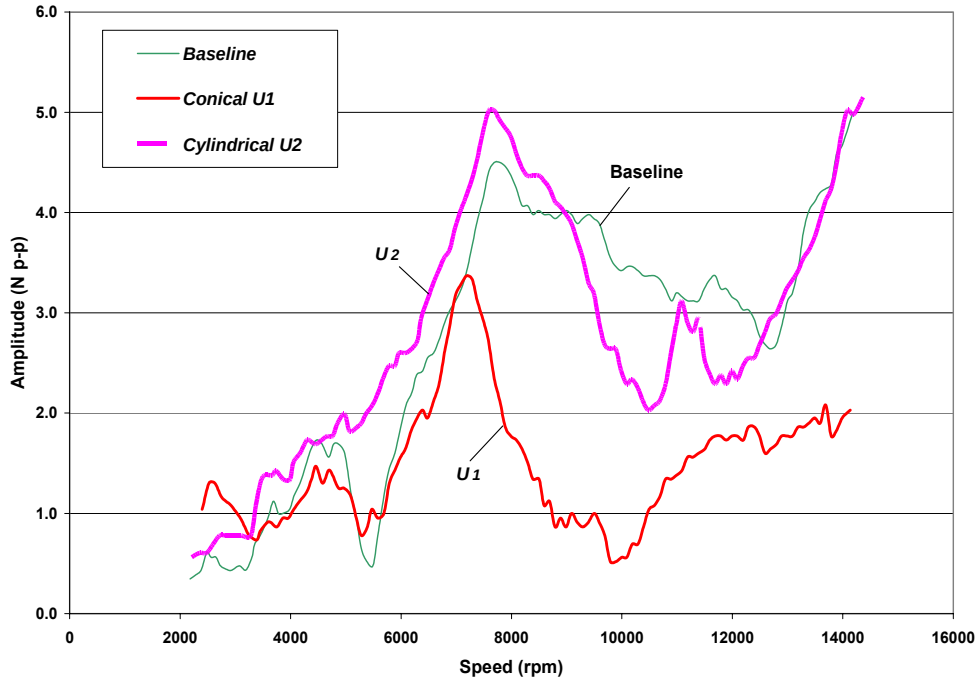

Fig. 26 Synchronous bearing transmitted load peak-peak amplitudes for the rotor baseline and calibrated imbalance responses collected at the left bearing plane, 120° clockwise to the vertical direction. No external supply gas pressure. Test bearing set #2

Post inspection of the test rotor and bearings

The rotor and bearings were inspected after the coastdown tests. Wear of the solid surfaces was evident due to the frequent start-up and shutdown tests. The NFC (Near-Frictionless Carbon) coating layer on the rotor was damaged during testing and coating residue was attached to the inner surface of the bearing. Table 6 summarizes the radial clearance variations after each test series. Recall that coastdown tests were conducted first with bearing set #1 with the NFC coating in its original condition. The rotor wear due to coastdown tests with this bearing pair damaged the NFC coating, enlarging the radial clearance for the other bearing pair from its original radial clearance of 23 μm to ~ 26 μm. The clearance variation for the secondly tested bearing (set #2) is quite large as all the coating layer was completely destroyed after the tests. Metal from

the steel shaft and bearings was also removed because the rubbing was too severe and sustained at low shaft speeds.

Table 6 Bearing radial clearances for the tests

Parameters	*Bearing set #1*		*Bearing set #2*	
	B1	B2	B1	B2
Measured radial clearance prior to tests	36 ± 3	37 ± 3	26 ± 3[8]	28 ± 3[8]
Actual radial clearance after test completion	39 ± 3	39.45 ± 3	30 ± 3	31.25 ± 3
Percentage of variation	6.8%	6.7%	15%	14%

Additionally, due to rotor magnetizing, a cogging torque phenomenon, accompanied by wide broad band frequency (rubbing) and rattle noise at a constant speed rotor operation occurred. The cogging torque is produced by the magnetic attraction between the rotor armature and the motor stator. This phenomenon appeared with test bearing set #2. Actually, the electrical insulation of the motor stator was damaged during the repeat start/stop rotor operation. This may have contributed to the rotor magnetizing. However, the motor drive torque vanishes when the rotor coasts down since the electrical motor is off. The rattle noise and small amplitude broad band frequency (rubbing) disappeared immediately. Table 7 lists the residual magnetism of the rotor. One Gauss (G) is one line of flux passing through at 1 cm^2 area. Although residual magnetism is not considerable, the manufacturer recommends reducing the residual magnetism to its lowest level possible.

Table 7 Residual magnetism of the rotor

Residual Magnetism (Gauss)	Armature	Left Sleeve	Right Sleeve
Before the test	± 2		
After the test	-2 ~ -15	-1 ~ -6	4 ~ 6

[8] Measured after the rotor tests with bearing set #1

Estimation of the gas bearing equivalent stiffness

The gas bearing equivalent stiffness K_{eq} can be obtained from the system critical speed (ω_c) and the rotor mass shared by each bearing (M_1=*0.435 kg*), i.e. $K_{eq} = M_1 \omega_c^2$. Table 8 gives the critical speeds and equivalent stiffness determined from the rotor remnant imbalance responses (including slow roll vector subtraction) for various feed pressures. Figure 27 displays the critical speeds for test bearings, set #1 and set #2 respectively. Designation in the plot of LH and LV correspond to the rotor motion planes at the left bearing end, horizontal and vertical, respectively. A similar notation follows for the right bearing end, RH and RV. The critical speeds are proportional to the supply pressures for both test bearings. Figure 28 shows the gas bearing equivalent stiffness also increases with increasing supply pressures. The external supply gas pressures stiffen the rotor-bearing system. The various stiffness at each plane results in different critical speeds. In addition, Figure 27 and Figure 28 show the comparison of critical speeds and equivalent stiffness for both test bearing sets. The bearing set #2 with smaller radial clearance provides more stiffness and increases the critical speed of the rotor-bearing system.

Estimation of damping ratios

When appropriate, the Q factor method can be used to estimate the viscous damping ratio (ζ) of the rotor on its bearings. Figure 29 shows a typical rotor response and the nomenclature for application of the method. The Q-factor and damping ratio (ζ<0.1) are defined for slightly damped systems as:

$$Q = \frac{N_n}{N_2 - N_1} \qquad \zeta = \frac{1}{2Q} \tag{2}$$

Table 8 Identification of critical speeds and equivalent stiffness from the baseline imbalance response

Name	Absolute Supply Pressure (bar)	Critical speed[9] (rpm)		Equivalent stiffness K_{eq} (MN/m) (±0.02 MN/m)	
		Bearing actual radial clearance		Bearing actual radial clearance	
		Set #1 31.25 μm	Set #2 39.45 μm	Set #1 31.25 μm	Set #2 39.45 μm
LV- Left bearing vertical plane	1.01	5,970	-	0.17	-
	2.39	7,090	5,700	0.24	0.15
	3.77	7,290	6,290	0.25	0.19
	5.15	7,690	6,900	0.28	0.23
LH - Left bearing horizontal plane	1.01	6,590	-	0.21	-
	2.39	*[10]	5,590	*[10]	0.15
	3.77	6,990	6,390	0.23	0.19
	5.15	7,690	6,900	0.28	0.23
RV- Right bearing vertical plane	1.01	7,290	-	0.25	-
	2.39	*[10]	5,700	*[10]	0.15
	3.77	8,100	5,590	0.31	0.15
	5.15	8,890	6,090	0.38	0.18
RH- Right bearing horizontal plane	1.01	6,890	*[10]	0.23	-
	2.39	*[10]	6,290	*[10]	0.19
	3.77	7,990	5,790	0.30	0.16
	5.15	8,600	6,490	0.35	0.20

[9] Uncertainty for critical speeds identification is about ±3% of shaft speed.

[10] The displacement peak amplitude is not obvious (too broad or multiple peaks) to identify a critical speed.

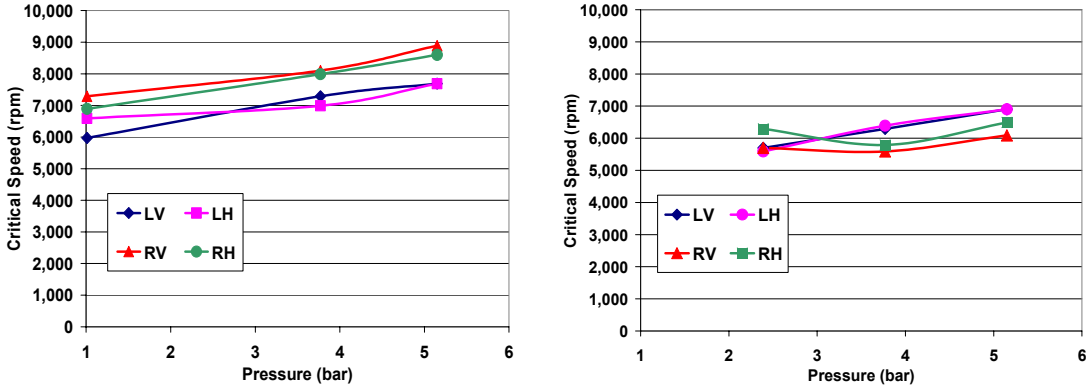

a) Bearing set #2, actual radial clearance 31.25 μm b) Bearing set #1, actual radial clearance 39.45 μm

Fig. 27 Critical speeds of the rotor-Rayleigh step gas bearing system versus gas supply pressure. LV- Left bearing, vertical plane; LH- Left bearing, horizontal plane; RV- Right bearing, vertical plane; RH- Right bearing, horizontal plane

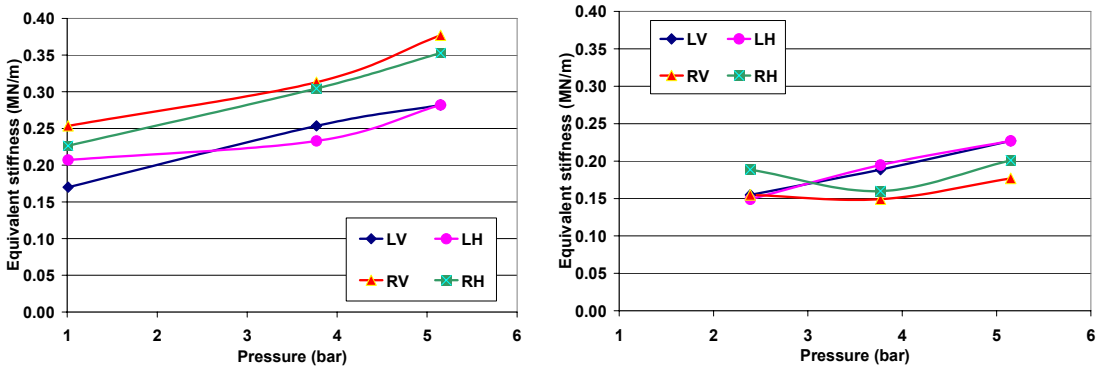

a) Bearing set #2, actual radial clearance 31.25 μm b) Bearing set #1, actual radial clearance 39.45 μm

Fig. 28 Estimated equivalent stiffness of the Rayleigh step gas bearing versus gas supply pressures. LV- Left bearing vertical plane; LH- Left bearing, horizontal plane; RV- Right bearing, vertical plane; RH- Right bearing, horizontal plane

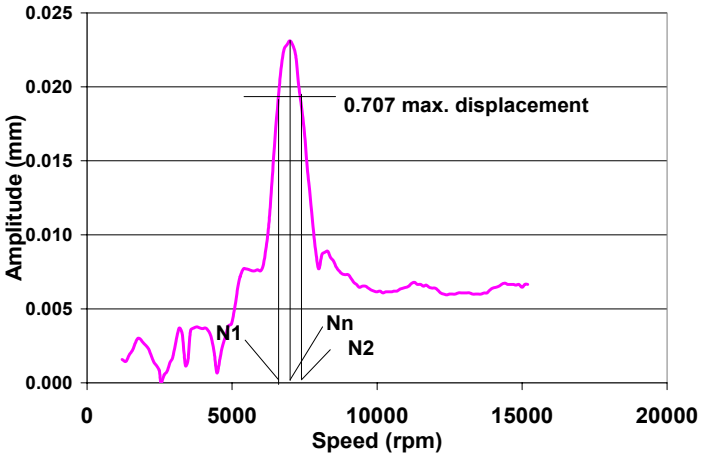

Fig. 29 Notation for application of *Q* factor method and estimation of damping ratio in gas bearing

Table 9 presents the gas bearing damping ratios determined from the baseline imbalance responses for various supply gas pressures. The damping ratios are in the range of 5% to 15%. The damping ratios are only identified for test bearings set #2. For the other bearing planes and test bearing set #1, multiple peaks or broad peak response around an expected critical speed region made it difficult to identify properly the damping ratio.

Figure 22 depicts these typical conditions at supply pressure of 2.39 bar and 1.01 bar. At the test pressure of 2.39 bar, multiple peaks around the critical speed region of 7 krpm may indicate a combined conical and cylindrical mode operation of the test rotor. The broad peak around the critical speed region (See the response at 1.01 bar around 7 krpm in Figure 22) demonstrates the rotor-bearing system has a good damping capability at this speed region. Note the damping ratio increases at the supply pressure at 5.15 bar than at 3.77 bar in Table 9. Recall that the displacement amplitudes increase with supply pressure shown in Figure 22, indicating the damping ratios drop for a higher supply pressure. The decrease in damping ratio is possibly due to the increasing system stiffness.

Table 9 Identified damping ratios from baseline imbalance responses for test bearing set #2

Displacement sensor	Absolute Supply Pressure (bar)	Damping Ratio[11]
LV Left Bearing Vertical Plane	2.39	--
	3.77	0.068
	5.15	0.149
LH Left Bearing Horizontal Plane	2.39	0.117
	3.77	0.057
	5.15	0.138

Threshold speeds of rotor instability

Rotordynamic instability is investigated with run-up tests to capture the onset threshold speed for various gas supply pressures. The measurements were conducted by slowly increasing the motor speed at a constant gas supply pressure. A two-channel real time frequency analyzer aids to display the displacement amplitude in the frequency domain. The instability onsets depend on the combined hydrodynamic and hydrostatic gas film bearing effects on the rotor dynamics. Threshold speeds are determined when the subsynchronous vibration magnitudes are half or larger than the synchronous response amplitudes displayed in a spectrum analyzer. The subsynchronous vibrations sustain and increase when the speed increases, deteriorating the reliability of the rotor-bearing system.

Figure 30 depicts a typical frequency spectrum of the rotor response on test bearing set #1 when a threshold speed of instability sets in. The whirl frequency locates where the large subsynchronous amplitude arises. The rotational speed is the threshold speed of instability. Threshold speeds are directly obtained from the readout of a tachometer, as the DAQ system (ADRE® or Labview®) shows an inaccurate speed due to the speed interval configuration.

[11] Uncertainty in damping ratio estimation is ~20%.

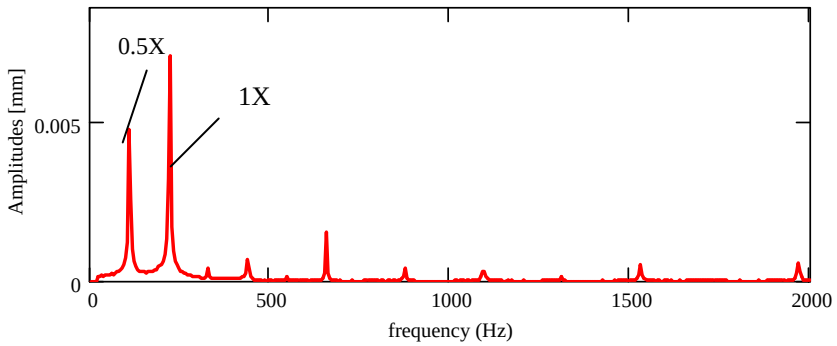

Fig. 30 A typical frequency spectrum to identify the threshold speed of instability on test bearing set #1. Data collected at left bearing, horizontal plane, for rotor speed of 13 krpm.

Table 10 and Figure 31 show the experimentally found threshold speeds of instability versus supply gas pressures for both test bearing sets. Threshold speeds display a slight decrement against increases in feed pressures below 4.8 bar (55 psig); then increase slightly. Whirl frequencies are fixed at 120 ± 4 Hz and 124 ± 4 Hz, respectively for test bearing set #1 (39.45 μm radial clearance) and bearing set #2 (31.25 μm radial clearance), approximately coinciding with the rotor-bearing system natural frequencies. For the test bearing set #1 without supply gas pressure, the instability sets in at a larger rotor speed than for the hybrid condition; demonstrating supply pressures weaken the stability of the rotor-bearing system as the gas supply decreases the rotor operating eccentricity on its bearing. The threshold speed for the condition of no gas supply pressure on test bearings set #2 could not be identified as severe rubbing occurred when increasing the shaft speed above 16 krpm. Note the rotor threshold speeds for test bearing set #2 are lower than for bearings set #1. One possible reason for the measured reduced threshold speeds is due to imperfect rotor-bearing alignment.

A whirl frequency ratio is defined as the ratio between the instability subsynchronous frequency and the frequency of rotation speed. Table 10 shows the whirl frequency ratios, ~ 0.5, and slightly larger for test bearings set #2. Whirl frequency ratios depend slightly on the test pressures.

Table 10 Experimentally determined threshold speeds of instability and whirl frequency ratios

Absolute Supply Pressure (bar)	Threshold Speed of Instability (rpm)		Whirl Frequency Ratio	
	Bearing Radial Clearance		Bearing Radial Clearance	
	Set #1 *39.45μm*	*Set #2* *31.25μm*	*Set #1* *39.45μm*	*Set #2* *31.25μm*
1.01	25,726	-	0.280	-
1.70	24,058	15,973	0.299	0.466
2.05	22,343	14,907	0.322	0.499
2.39	22,420	14,722	0.321	0.505
2.74	21,663	15,127	0.332	0.492
3.08	21,252	15,273	0.339	0.487
3.43	21,558	14,797	0.334	0.503
3.77	21,078	14,564	0.341	0.511
4.12	21,023	14,546	0.342	0.512
4.46	20,906	14,497	0.344	0.513
4.80	20,950	14,533	0.344	0.512
5.15	21,063	14,662	0.342	0.507
5.49	21,610	14,766	0.333	0.504

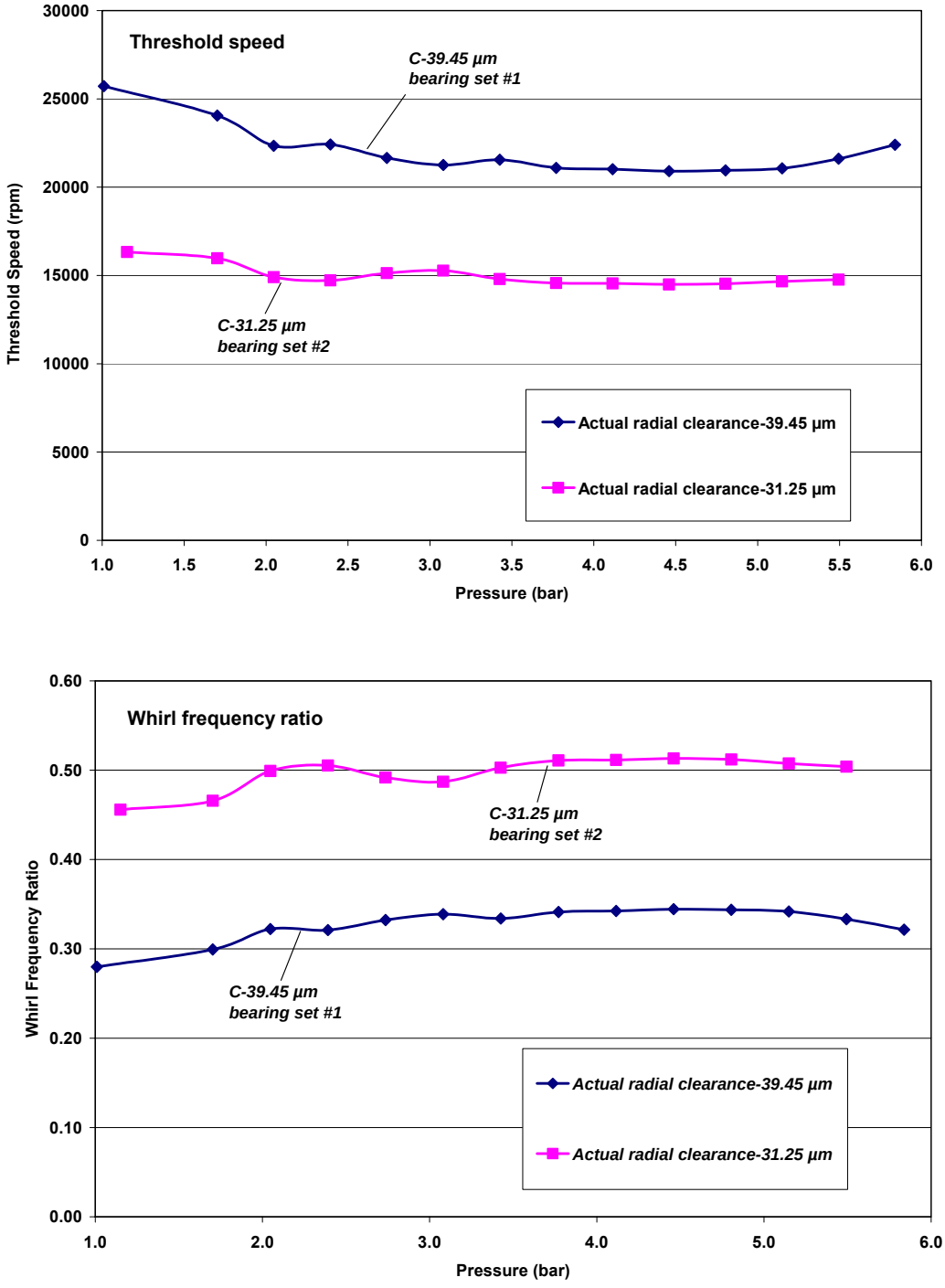

Fig. 31 Threshold speeds of instability and whirl frequency ratios versus supply gas pressures for two test bearing sets.

Closure for Experimental Responses of the Rotor Supported on Rayleigh Step Bearings

The recorded coastdown responses of the test rotor on Rayleigh step bearing provide meaningful information on its rotor dynamic performance. Imbalance responses were recorded at increasing supply gas pressures, up to five times ambient. An external supply gas pressure is required to ensure early rotor liftoff and reduce rubbing at rotor start-up and shutdown. However, the rotor still experienced dry friction contact at low speeds as the gas film in the bearings could not support the rotor. Critical speeds are identified, when possible, at clearly defined synchronous displacement peak responses to imbalance with a 180° phase change. The *Q*-factor method was used to evaluate damping ratios at the critical speeds. Identified damping ratios vary from 5% to 15% depending on the feed pressures. The experimental responses demonstrate feed gas pressures increase the system first critical speed and decrease the damping ratio, thus verifying similar characteristics as with other gas bearings tested earlier [6, 7]. The critical speed is higher for the test bearing with a tighter clearance (bearing set #2). A 2^{nd} critical speed was found for test bearings set #1. Increasing feed pressures decreases the 2^{nd} critical speed, as shown in Figure 14.

Measured bearing transmitted loads display considerable 4X supersynchronous components over the test speed range due to the time-varying pressure field, resulting from the four rotating groove-pads. External feed gas pressures enlarge the magnitudes of the 4X transmitted loads. Incidentally, the synchronous bearing transmitted loads show low magnitudes over the test speed range even at the critical speed regions. The overall transmitted loads reach 35 N at a test pressure of 5.15 bar for test bearing set #1 when approaching the critical speed region.

The test rotor on the Rayleigh step bearing set #2 shows stable operation without hydrostatic pressurization below 15 krpm. No rubbing exists in the speed range of 4-14.5 krpm, demonstrating the rotor operates on a hydrodynamic film developed by the gas bearings. The threshold speeds of instability depend slightly on the supply gas pressures. Test bearing set #1 with a larger clearance has a higher measured threshold speed of ~25

krpm or less. Experiments demonstrate a purely hydrodynamic operation condition gives a slightly higher threshold speed of instability than for the hybrid pressurized condition. The whirl frequency at instability is fixed at approximately the rotor-bearing system natural frequency (~ 120 Hz). Whirl frequency ratios are ~ 0.33 and ~ 0.5 for bearing set #1 and set #2, respectively.

PREDICTION OF ROTORDYNAMIC PERFORMANCE OF TEST ROTOR SUPPORTED ON RAYLEIGH STEP GAS BEARINGS

Rotordynamic performance predictions of the test gas bearings are obtained using a two dimensional finite element model [37] solving Reynolds equation for gas films. Predictions are applicable for hydrodynamic conditions without supply gas pressure. The finite element analysis determines the pressure profiles and predicts steady state bearing performance including journal eccentricities, power consumption, as well as rotordynamic force coefficients. Synchronous bearing force coefficients are then integrated into a rotor structural model in XLTRC^2 to predict the rotor-bearing dynamic performance. The synchronous rotor response to imbalance shows the rotor performance when traversing a critical speed. Frequency dependent force coefficients are employed to predict the critical mass and whirl frequency ratio at the rotor-bearing instability threshold. Predictions are compared to the experimental results.

Figure 32 shows the schematic geometry of Rayleigh step bearing/rotor and a coordinate system in the bearing middle plane[12]. The bearing has length L and radial clearance C. The journal has eccentricity (e_X, e_Y) when rotating at an angular speed Ω. The geometry for each pad includes the Rayleigh step and ridge. Axial grooves separate the Rayleigh steps. Table 11 summarizes the parameters describing the geometry for the bearings and rotor as well as operating conditions. Note that actual bearing radial clearances, rather than the nominal values, are used in the predictions considering the rotor wear after the tests were completed.

[12] Rayleigh steps and grooves are assumed on the bearings for the current analysis. A hydrodynamic pressure analysis with steps and grooves on the rotor surface has been completed, not used yet due to the author's ignorance.

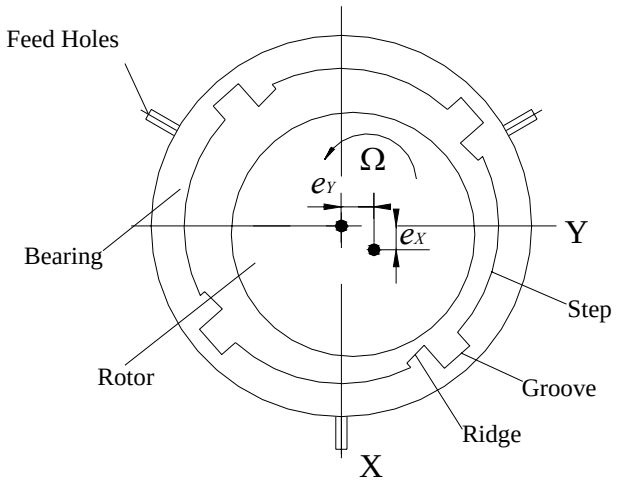

Fig. 32 Schematic view of geometry for rotor performance predictions with supported Rayleigh step bearings

Table 11 Geometry and operating conditions for analysis of Rayleigh step bearings/rotor performance

Parameters	***Values***		***Units***
	Bearing set		
	1	2	
Bearing radial clearance in analysis	39.45	31.25	μm
Step diameter	28.90		mm
Step angle	64.9		degrees
Step arc length	16.4		mm
Step number	4		N/A
Pad angle	78.1		degrees
Ambient temperature, T	298.15		K
Ambient pressure, P_A	1.01×10^{5}		Pa
Gas viscosity at ambient condition, μ	1.86×10^{-5}		Pa-s
Gas density at ambient condition , ρ_A	1.21		kg/m^3

The steady-state Reynolds equation for isothermal, inertialess and isoviscous ideal gas flow is

$$\frac{\partial}{\partial x}\left(\frac{Ph^3}{12\mu}\frac{\partial P}{\partial x}\right)+\frac{\partial}{\partial y}\left(\frac{Ph^3}{12\mu}\frac{\partial P}{\partial y}\right)=\frac{\Omega\cdot R}{2}\frac{\partial(Ph)}{\partial x}+\frac{\partial(Ph)}{\partial t} \tag{3}$$

where the film thickness h is given by

$$h = C_f + e_X\cos\theta + e_Y\sin\theta \tag{4}$$

$C_f\ (\theta)$ is the radial clearance along the bearing circumferential direction, depending on the position at steps, ridges and grooves. The nomenclature gives the definitions for all parameters. The pressure at the grooves equals ambient.

Predicted Dynamic Performance of Rotor/Bearing System

Figure 33 shows the predicted journal eccentricities for both bearing sets with radial clearances *(C)* of 31.25 μm and 39.45 μm, respectively. The applied static load is half of the rotor weight, i.e. 4.26 N. Eccentricities are large over the shaft speed range. At low speeds, eccentricities are nearly equal to the bearing clearance. Evidently rubbing will happen in actual operation. The journal eccentricity is smaller for the bearing with less clearance. Figure 34 depicts nearly constant journal attitude angles over the speed range considered. The bearing with a larger clearance shows the larger attitude angle, Figure 35 shows the power loss due to shear friction in both bearings, being of similar magnitudes.

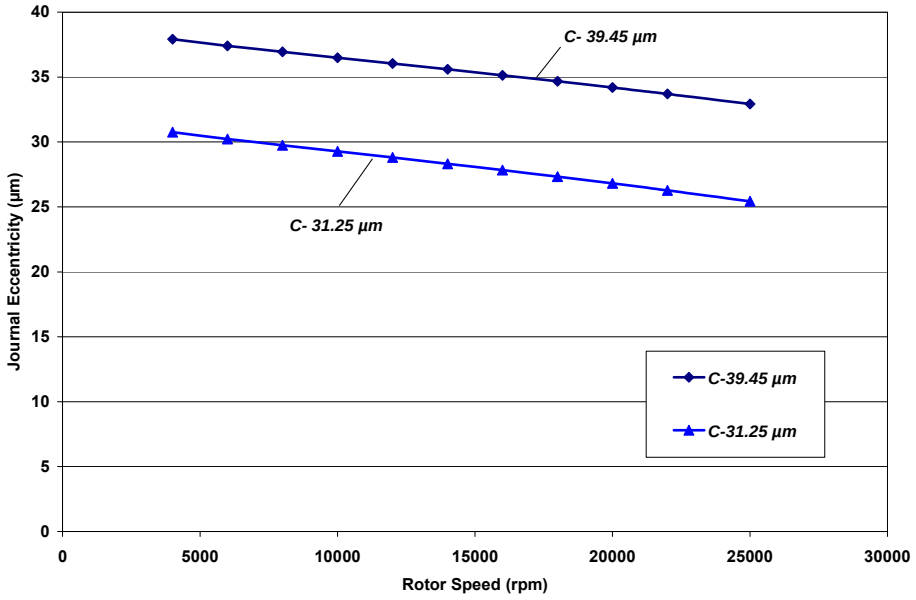

Fig. 33 Predicted journal eccentricities versus rotor speeds for bearings with radial clearances (*C*) of 39.45 µm and 31.25 µm

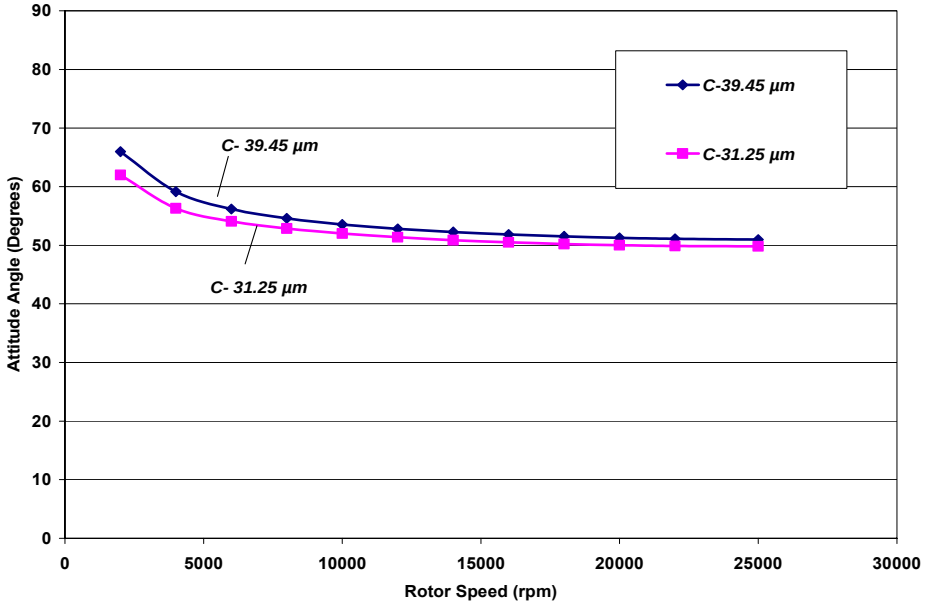

Fig. 34 Predicted attitude angles versus rotor speeds for bearings with radial clearances (*C*) of 31.25 µm and 39.45 µm

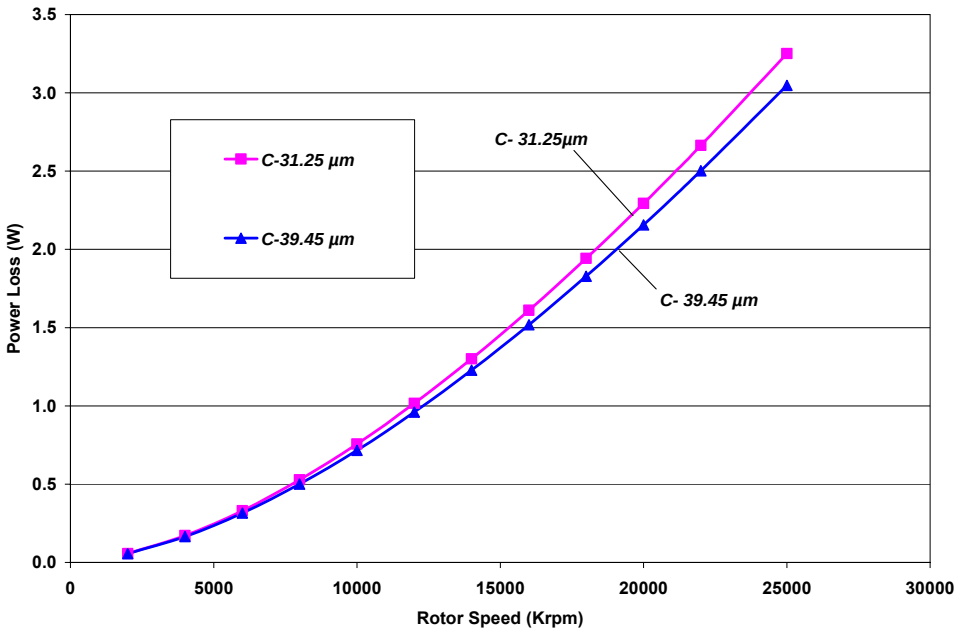

Fig. 35 Predicted power loss for bearings with radial clearances (*C*) of 31.25 µm and 39.45 µm, respectively

Figure 36 displays the static (zero excitation frequency) stiffness coefficients versus rotor speeds for two bearing sets. Direct stiffness coefficients, K_{XX} and K_{YY}, decrease considerably as speed increases and approach similar magnitudes of around 0.3 MN/m at high speeds. Cross-coupled stiffness coefficients K_{XY} and K_{YX} also decrease with rotor speeds. K_{YX} becomes negative at the highest speed.

Figure 37 shows the synchronous speed stiffness coefficients for both bearings. Direct synchronous stiffness coefficients K_{XX} drop rapidly from 10 MN/m until approaching the rotor speed of 10 krpm. The synchronous stiffness vary moderately at high rotor speeds. Both bearings exhibit similar synchronous stiffness magnitudes at high rotor speeds. Synchronous speed dynamic stiffness coefficients have larger magnitudes compared to the static stiffness coefficients, shown in Figure 36.

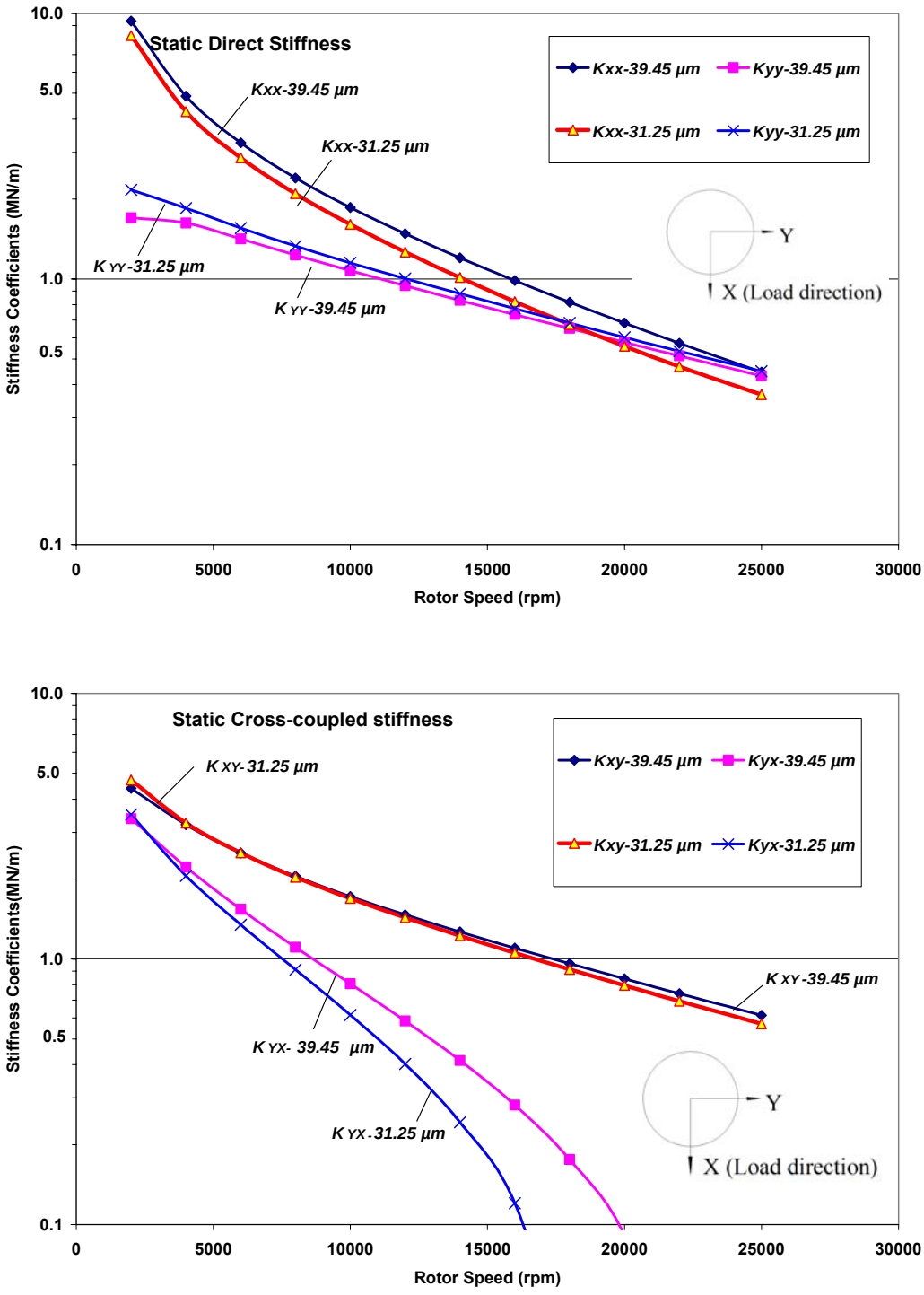

Fig. 36 Predicted static direct and cross-coupled stiffness coefficients for bearings with radial clearances (*C*) of 31.25 µm and 39.45 µm

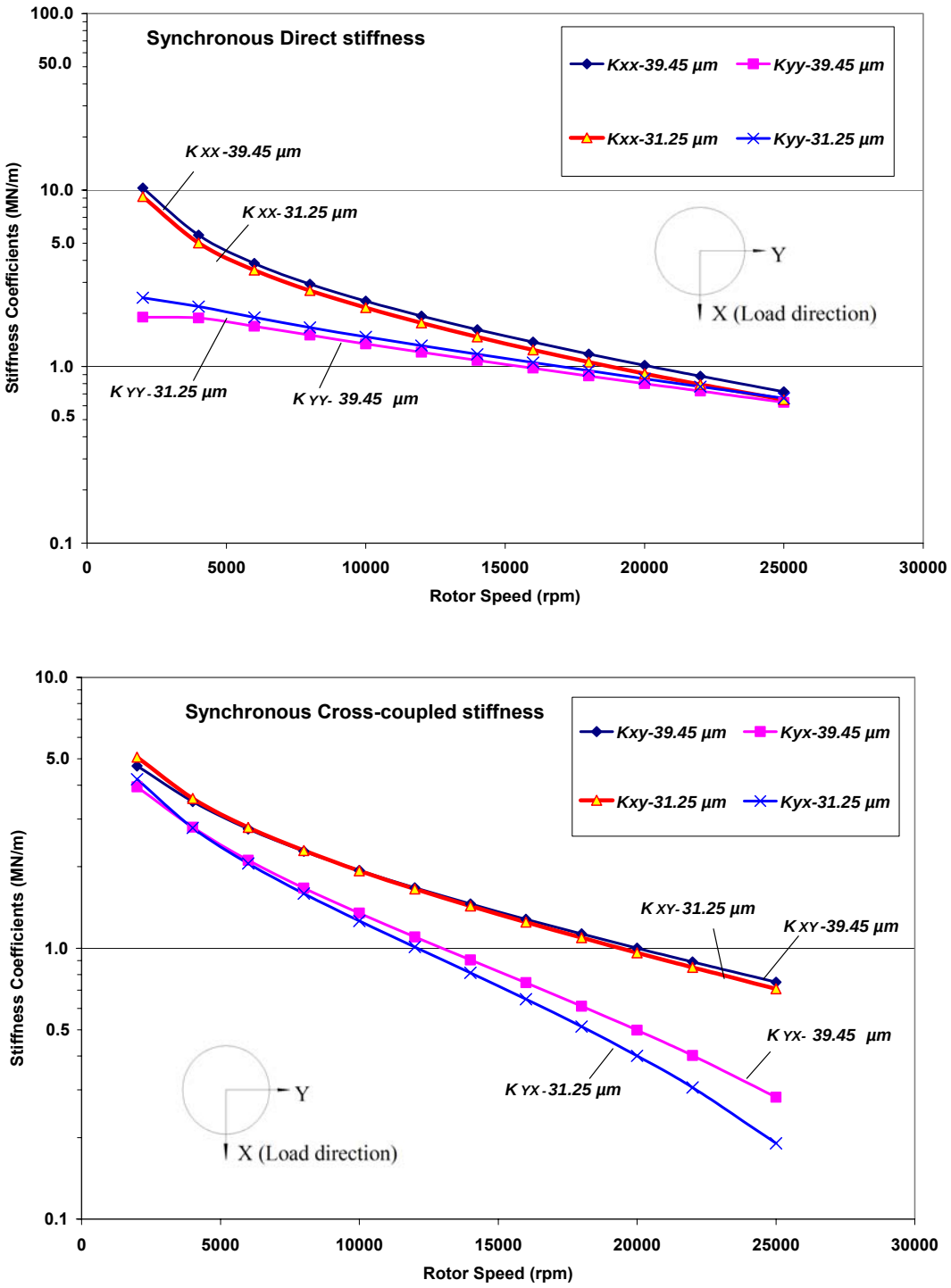

Fig. 37 Predicted synchronous direct and cross-coupled stiffness coefficients for bearings with radial clearances (*C*) of 31.25 µm and 39.45 µm

Figure 38 depicts the synchronous speed damping coefficients, decreasing with rotor speeds for both bearing sets with radial clearances *(C)* of 31.25 μm and 39.45 μm, respectively. Note the damping coefficients have small magnitudes at high speeds, indicating a reduced capability in attenuating vibrations.

Figure 39 depicts the predicted bearing equivalent stiffness coefficients[13] K_{eq} are 0.23 MN/m for bearing set #1 (radial clearance of 39.45 μm), and 0.25 MN/m for bearing set #2 (radial clearance equal to 31.25 μm). Equivalent stiffness coefficients are nearly constant over the speed range. Note that identified equivalent stiffness coefficients from the measurements, shown in Table 8, are smaller than the predictions. The critical speeds can be obtained from the predicted equivalent stiffness (K_{eq}) and half of the rotor mass (M_1), i.e., $\omega_c = (K_{eq}/M_1)^{0.5}$. Table 12 shows the predicted critical speeds and comparison with experimentally identified values. Predictions show higher critical speeds than in the tests. The possible reason for the difference is due to the present model limitations considering grooves and steps etched on the bearings rather than on the journal. In addition, note that the actual bearings' clearances at the time when the experiments were conducted are unknown.

Table 12 Predicted and experimentally identified critical speeds. Experimental data correspond to the test pressure of 2.39 bar, at left bearing vertical plane. Predictions without hydrostatic feed pressure effects

	Bearing Radial Clearance (set #1) 39.45 μm	Bearing Radial Clearance (set #2) 31.25 μm
Predicted critical speed (rpm)	~6,600	~7,200
Experimental identified critical speed (rpm)	5,590	6,590
Percentage of difference	18%	9%

[13] $K_{eq} = (K_{XX}C_{YY} + K_{YY}C_{XX} - C_{YX}K_{XY} - C_{XY}K_{YX})/(C_{XX} + C_{YY})$

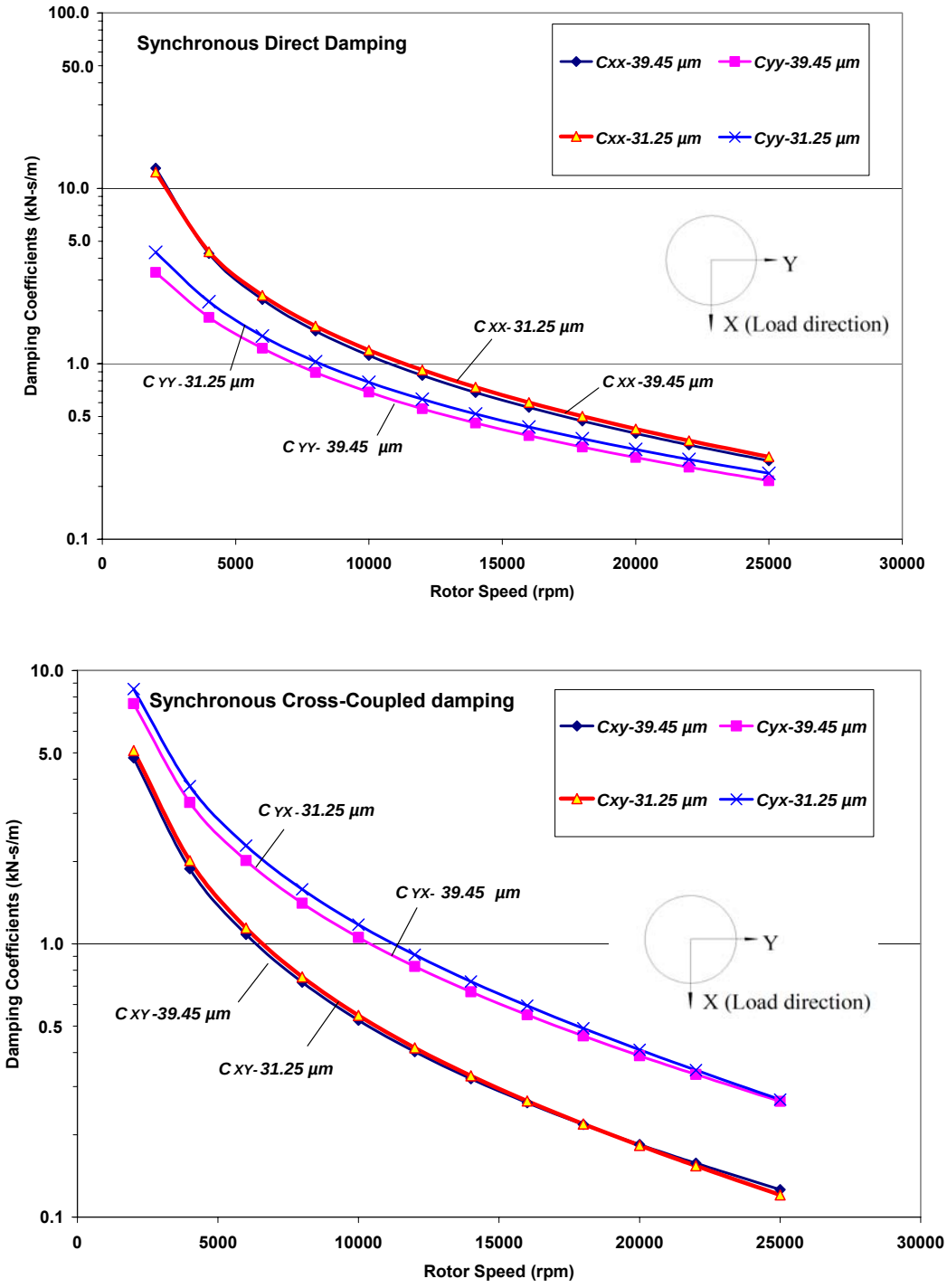

Fig. 38 Predicted synchronous direct and cross-coupled damping coefficients for bearings with radial clearances (*C*) of 31.25 µm and 39.45 µm

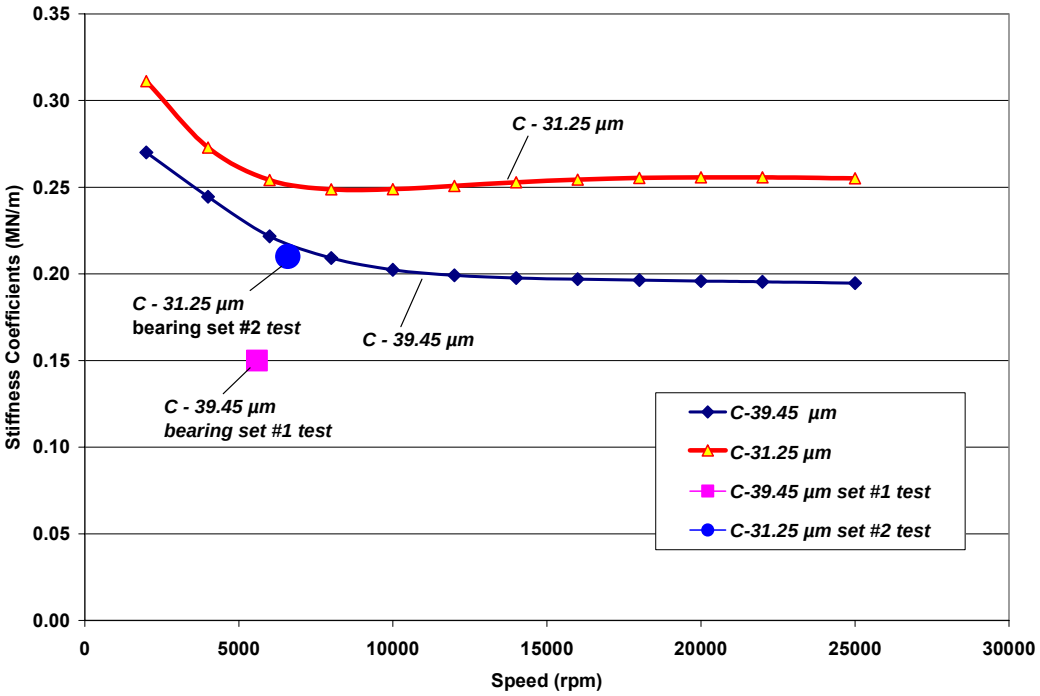

Fig. 39 Predicted synchronous equivalent stiffness coefficients K_{eq} for bearings with radial clearances (C) of 31.25 µm and 39.45 µm, respectively.

Figure 40 displays the effects of excitation frequency on the bearing dynamic stiffness coefficients for a rotor speed of 10 krpm. The vertical line in the figure indicates the rotor operation speed. Direct stiffness coefficients K_{XX} and K_{YY} increase with excitation frequency, becoming about twice larger at four times the synchronous frequency than at 25% of synchronous speed. Excitation frequencies also increase the cross-coupled stiffness coefficients K_{XY} and K_{YX}. Excitation frequencies evidently stiffen the bearings. Figure 41 shows the damping coefficients versus excitation frequency for the modeled bearings. Damping coefficients decrease significantly with the excitation frequency, and approaching small values at high excitation frequencies.

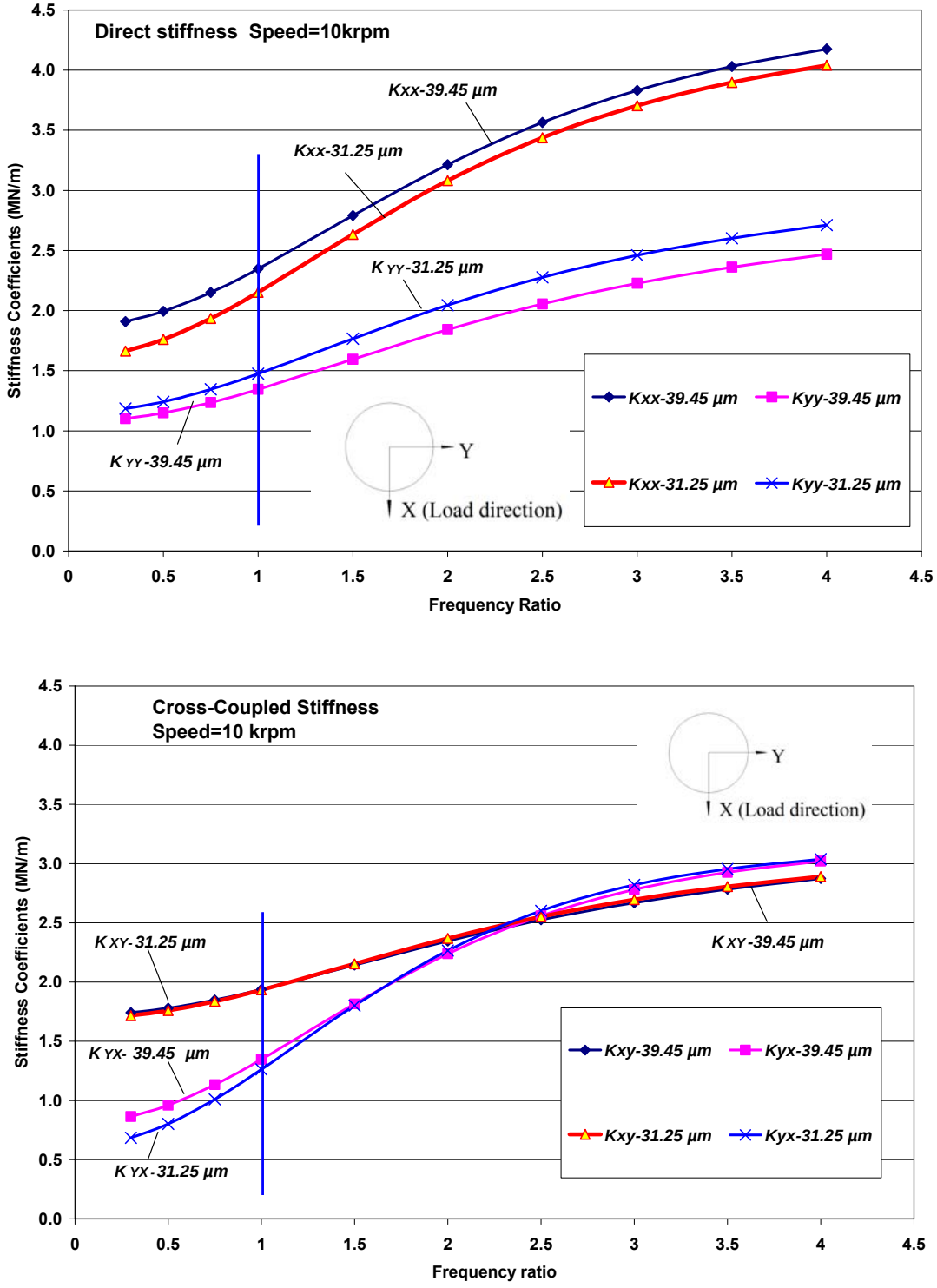

Fig. 40 Predicted effect of excitation frequency on bearing stiffness coefficients for rotor speed of 10 krpm. Bearings with radial clearances (*C*) of 31.25 µm and 39.45 µm

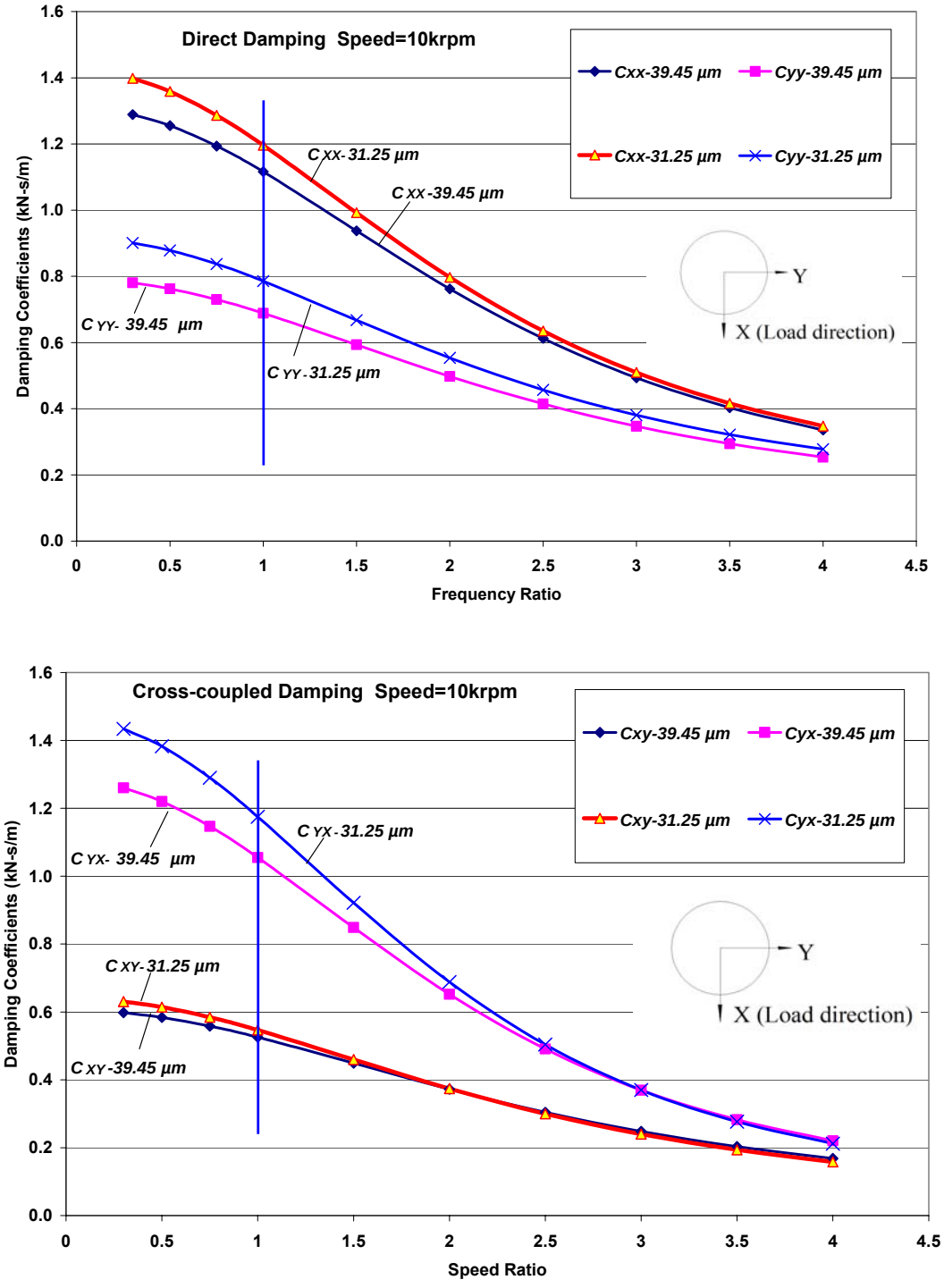

Fig. 41 Predicted effect of excitation frequency on bearing damping coefficients for rotor speed of 10 krpm. Bearings with radial clearances (*C*) of 31.25 µm and 39.45 µm

Rotordynamic instability was investigated using Lund's method [38]. The differential equations for a point mass rotor, perfectly balanced, supported on bearings are

$$\begin{aligned} M_R\ddot{X} + C_{XX}\dot{X} + C_{XY}\dot{Y} + K_{XX}X + K_{XY}Y = 0 \\ M_R\ddot{Y} + C_{YY}\dot{Y} + C_{YX}\dot{X} + K_{YY}Y + K_{YX}X = 0 \end{aligned} \tag{5}$$

where M_R is ½ the system mass, C_{ij} *(i,j=X, Y)* and K_{ij} *(i,j=X, Y)* are gas bearing damping and stiffness coefficients, respectively. The general solution of equation (5) is

$$X = Ae^{st}, \qquad Y = Be^{st} \tag{6}$$

where s is an eigenvalue, and A and B are constants determined by initial conditions in displacement and velocity. The characteristic equation of (5) is

$$\begin{bmatrix} M_R s^2 + C_{XX}s + K_{XX} & K_{XY} + C_{XY}s \\ K_{YX} + C_{YX}s & M_R s^2 + C_{YY}s + K_{YY} \end{bmatrix} \begin{Bmatrix} A \\ B \end{Bmatrix} = 0 \tag{7}$$

A non-trivial solutions exists when the determinant is zero which defines two roots,

$$s = a \pm i\omega \tag{8}$$

where a is the damping component and ω is the damped natural frequency. If $a > 0$, the rotor motion grows with time and the rotor-bearing system becomes unstable. At the threshold speed of instability, the eigenvalue has the form of $s = \pm i\omega$. Define the bearing impedance coefficients as

$$\begin{aligned} Z_{XX} &= K_{XX} + i\omega C_{XX} & Z_{XY} &= K_{XY} + i\omega C_{XY} \\ Z_{YX} &= K_{YX} + i\omega C_{YX} & Z_{YY} &= K_{YY} + i\omega C_{YY} \end{aligned} \tag{9}$$

where the frequency dependent force coefficients are determined from the preceding FE model [35]. Substitution of equations (8) and (9) into equation (7) generates

$$\begin{bmatrix} Z_{XX} - M_R\omega^2 & Z_{XY} \\ Z_{YX} & Z_{YY} - M_R\omega^2 \end{bmatrix} \begin{Bmatrix} A \\ B \end{Bmatrix} = 0 \tag{10}$$

The determinant of the matrix in equation (10) is

$$\Delta = (Z_{XX} - M_R\omega^2)(Z_{YY} - M_R\omega^2) - Z_{XY}Z_{YX} = 0 \tag{11}$$

Define $Z_M = \omega^2 M_R$. From equation (11)

$$Z_M(\omega) = 0.5(Z_{XX} + Z_{YY}) - [0.25(Z_{XX} - Z_{YY})^2 + Z_{XY}Z_{YX}]^{0.5} = K_e + i\omega C_e \tag{12}$$

where K_e and C_e are effective stiffness and damping coefficients. The critical ½ rotor mass (M_R) at the threshold speed of instability is determined when the effective damping C_e equals zero. Rotor critical masses and whirl frequency ratios are found for increasing shaft speeds. The rotor critical mass is the maximum mass which the gas film can carry at a rotor speed. The rotor will become unstable if the mass is larger than the critical mass at this speed.

Figure 42 depicts the predicted whirl frequency ratio (WFR) versus rotor speed. Note the WFRs vary slightly at high rotor speeds and have values around 0.6 ~ 0.7. Figure 43 shows the predicted critical mass (CM) to drop quickly as the shaft speed increases. The threshold speed is determined when the critical mass equals half of the rotor mass, i.e., 0.435 kg. Predictions indicate the rotor bearing system will become unstable above speeds equal to 8,363 rpm and 8,406 rpm for bearing set #1 and set #2, respectively. The predictions show much lower threshold speeds of instability than those found in the experiments (see Table 10) due probably to the limitations of the FE model which considers a grooved stator and smooth journal.

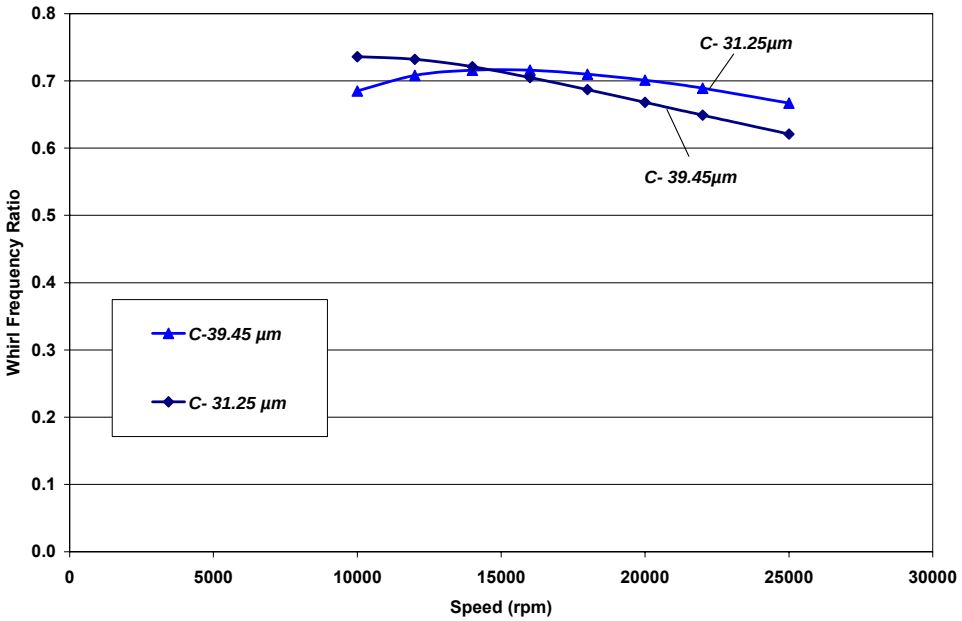

Fig. 42 Predicted whirl frequency ratio (WFR) versus rotor speed for bearings with radial clearances (*C*) of 31.25 µm and 39.45 µm.

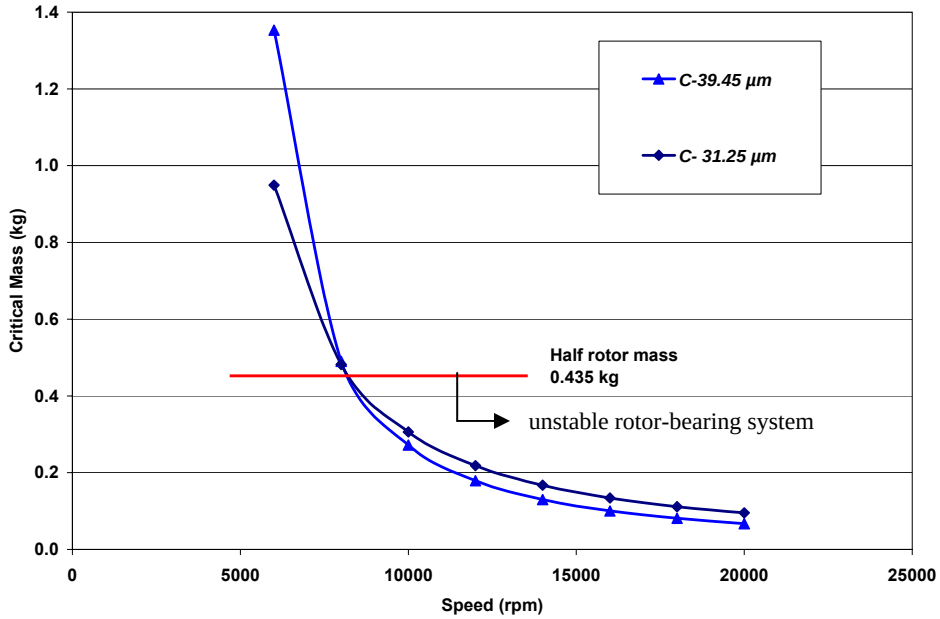

Fig. 43 Predicted critical mass versus rotor speed for bearings with radial clearances (*C*) of 31.25 μm and 39.45 μm.

Predictions of the Rotor/Bearing Performance with XLTRC^2

The physical model created with XLTRC^2 is shown in Figure 5. This model links synchronous bearing force coefficients to predict the imbalance response of a Rayleigh step rotor/bearing system.

Predicted imbalance responses to the calibrated imbalance mass

The imbalance mass for each rotor end is set to 1.5 g-mm[14] with conical excitation modes. Figure 44 shows the comparison of predicted imbalance displacement responses with supporting synchronous bearing force coefficients and experimental response to the remnant imbalance at the left bearing horizontal plane for the two sets of test bearings. The experimental imbalance responses correspond to a supply pressure of

[14] Recall that in the calibrated imbalance response tests with bearing set #2, the imbalance equals to 0.042 g × 12 mm = 0.504 g-mm (see page 33). Since the predicted rotor responses are comparable to the measurements, the imbalance mass used in the predictions probably accounts for the unknown remnant imbalance of the rotor.

1.15 bar for bearing set #2; and 2.39 bar for bearing set #1. The predictions show larger critical speeds for the bearings with smaller clearances, agreeing well with the experiments. Note that the predicted critical speeds are lower than the test baseline imbalance responses. In the tests, the hydrostatic pressurization increased the system stiffness and raised the critical speeds.

Closure on the Prediction of Rotordynamic Performance

A finite element lubrication model of the Rayleigh step gas bearing is employed to analyze the steady state and dynamic force performance of the bearings for a given static load. Pressure fields are found by solving classic Reynolds equation at steady state conditions. The journal eccentricities are determined at various rotor speeds. Frequency-dependent force coefficients are obtained from a small perturbation analysis. The static and synchronous force coefficients, stiffness and damping, decrease with increasing shaft speeds. Dynamic force coefficients show a strong dependency on the excitation frequency. Increasing the excitation frequency increases the bearing stiffnesses while decreases the damping coefficients.

The synchronous dynamic force coefficients are linked to a physical model generated by XLTRC^2 for imbalance response predictions. Critical speeds are predicted from synchronous imbalance responses. The rotor on bearing set #2, i.e. the bearings with smaller clearance, exhibits a larger critical speed. Predicted critical speeds agree well with the experimental measurements. Imbalance response predictions show similar behavior as the experimental coastdown responses. Predicted threshold speeds of instability are much lower than the experimental results due to the analytical model limitations, which consider a grooved stator and smooth journal bearing.

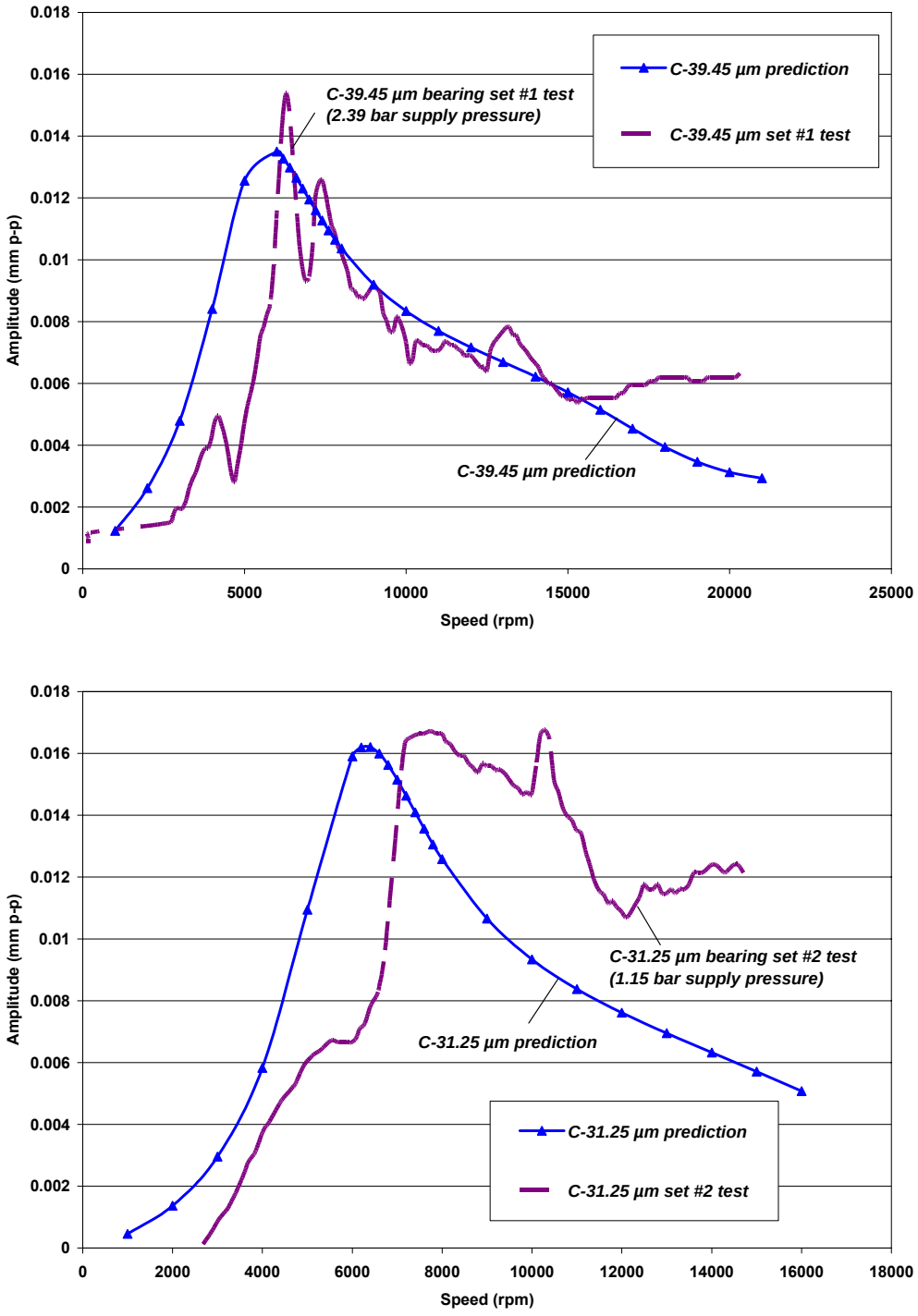

Fig. 44 Comparison of synchronous rotor displacement peak-peak amplitudes: predictions and test baseline at left bearing, horizontal plane. Test bearing sets with radial clearances (*C*) of 39.45 µm (top) and 31.25 µm (bottom).

CONCLUSIONS

The experimental investigation on a rotor supported on Rayleigh step hybrid gas bearings shows valuable information of its rotor dynamic performances. The rotor critical speeds, system damping ratios and onset speeds of rotor instability are determined for various feed gas pressures.

The Rayleigh step gas bearings exhibit adequate static load capacity to lift off the rotor without external pressurized air at shaft speeds above ~4 krpm. The near frictionless carbon (NFC) coating on the rotor surface reduces friction of the rotor against its bearings, extending the rotor coastdown time. However, rotor rubbing on its bearings occurred at shaft speeds below ~4 krpm since the gas bearings were not able to support the rotor weight. External pressurization provides additional stiffness to the rotor-bearing system and affects the rotor critical speeds and damping ratios. The rotor-bearings system critical speeds and damping ratios are identified at the rotor synchronous peak responses to imbalance. The rotor on the bearings with tighter clearances shows a higher critical speed.

The Rayleigh step gas bearing generates a time-varying pressure field due to the rotating groove-pads on the rotor configuration, thus determining a significant 4X supersynchronous component on the transmitted bearing loads. This phenomenon is further exacerbated by increasing the feed gas pressure. The synchronous components of bearing transmitted loads are small when compared to the 4X components over the test speed range (below 20 krpm). Severe rotor instabilities are found for various supply gas pressures. The threshold speed of instability depends slightly on the hydrostatic pressure. The rotor exhibits subsynchronous whirl at a shaft speed slightly larger for purely hydrodynamic operation than for the hybrid (hydrostatic pressurize) condition. The rotor could not be operated above 20 krpm.

The prediction of free-free mode natural frequency indicates rigid mode rotor modes over the test speed range. Measured rotor free-free natural frequencies are in agreement with predictions. Predictions using a finite element lubrication model give the

steady state and dynamic force coefficients of the Rayleigh step gas bearings for purely hydrodynamic conditions. Predicted power losses due to viscous shear friction are small, less than ~ 3 Watts for the gas bearings. The stiffness and damping coefficients decrease with shaft speed. Excitation frequencies show strong effects on the bearing dynamic force coefficients. Predicted synchronous imbalance responses show similar behavior as in the experimental measurements. The predicted system critical mass indicates a much lower onset threshold speed of instability, ~ 50% or less of the measurements due to the present model limitations with a grooved stator and smooth journal.

The present experiments and analysis show the application of Rayleigh step gas bearings for oil-free turbomachinery applications. The Rayleigh step gas bearings offer similar characteristics as other gas bearings tested earlier [6, 7], i.e., increased critical speeds and reduced damping ratios with increasing feed gas pressures. The Rayleigh step bearing has a rigid geometry and less tolerance to rotor misalignment, making the installation more difficult than with flexure pivot tilting pad bearings (FPTPBs) tested earlier [7]. Rayleigh step gas bearings show much lower operational speed ranges and threshold speeds of instability than FPTPBs. However, a FPTPB has a complex and costly construction. The present investigation demonstrates the Rayleigh step gas bearings are not reliable for high speed oil-free turbomachinery applications.

REFERENCES

[1] Barnett, M. A. and Silver, A., 1970, “Application of Air Bearings to High-speed Turbomachinery”, ASE Combined National Farm, Construction & Industrial Machinery and Powerplant Meetings, Milwaukee, WI, Paper #700720, pp. 1-8.

[2] Fuller, D. D., 1969, “A Review of the State-of-the-Art for Design of Self-Acting Gas-Lubricated Bearing”, ASME Journal of Lubrication Technology, **91**, pp. 1-16.

[3] Ehrich, F. F., and Jacobson, S. A., 2001, “Development of High-Speed Gas Bearings for High-Power Density Micro-Devices”, Proceedings of ASME Turbo Expo 2001, ASME Paper 2001-GT-0478, pp. 1-9.

[4] Szeri, A. Z., 1987, “Some Extensions of the Lubrication Theory of Osborne Reynolds”, ASME Journal of Tribology, **109**, pp. 21-36.

[5] Lund, J. W., 1967, “A Theoretical Analysis of Whirl Instability and Pneumatic Hammer for a Rigid Rotor in Pressurized Gas Journal Bearings”, ASME Journal of Lubrication Technology, **89**, pp. 154-163.

[6] Wilde, D. A., and San Andrés, L., 2003, “Experimental Response of Simple Gas Hybrid Bearings for Oil-Free Turbomachinery”, ASME Paper GT 2003-38833, pp. 1-11.

[7] Zhu, X, and San Andrés, L., 2004, “Rotordynamic Performance of Flexure Pivot Hydrostatic Gas Bearings for Oil-Free Turbomachinery”, ASME Paper GT 2004-53621, pp. 1-9.

[8] Jing, G., Zhang, L. P., and Hu, Z. Y., 1997, “On Fundamental Characteristics of a Hybrid Gas-Lubricated Journal Bearing with Surface-Restriction Compensation”, STLE Tribology Transactions, **40**, No. 3-4, pp. 528-535.

[9] Bonneau, D., Huitric, J. and Tournerie, B., 1993, “Finite Element Analysis of Grooved Gas Thrust Bearings and Grooved Gas Face Seals”, ASME Journal of Tribology, **115**, pp. 348-354.

[10] Denhard, W. G., and Pan, C. H. T., 1968, “Application of Gas-Lubricated Bearings to Instruments”, ASME Journal of Lubrication Technology, **90**, pp. 731-739.

[11] Wong, R. Y., Stewart, W. L., and Rohlok, H. E., 1968, “Pivot-Pad Journal Gas Bearing Performance in Exploratory Operation of Brayton Cycle Turbocompressor”, ASME Journal of Lubrication Technology, **90**, pp. 687-700.

[12] Fuller, D. D., 1984, *Theory and Practice of Lubrication for Engineers*, John Wiley & Sons, New York.

[13] Auloge, J. Y., Bourgin, P., and Gay, B., 1983, “The Optimum Design of One-Dimensional Bearings with Non-Newtonian Lubricants”, ASME Journal of Lubrication Technology, **105**, pp. 391-395.

[14] Archibald, F. R., and Hamrock, B. J., 1967, “The Rayleigh Step Bearing Applied to a Gas-Lubricated Journal of Finite Length”, ASME Journal of Lubrication Technology, **89**, pp. 38-46.

[15] Hamrock, B. J., 1968, “Rayleigh Step Journal Bearing, Part 1- Compressible Fluid”, ASME Journal of Lubrication Technology, **90**, pp. 271-280.

[16] Cunningham, R. E., Fleming D. P., and Anderson W. J., 1969, “Experimental Stability Studies of the Herringbone-Grooved Gas-Lubricated Journal Bearing”, ASME Journal of Tribology, **91**, pp. 52-57.

[17] Cunningham, R. E., Fleming D. P., and Anderson W. J., 1971, “Experimental Load Capacity and Power Loss of Herringbone Grooved Gas Lubricated Journal Bearings”, ASME Journal of Tribology, **93**, pp. 415-422.

[18] Faria, M. T. C., 2001, “An Efficient Finite Element Procedure for Analysis of High-Speed Spiral Groove Gas Face Seals”, ASME Journal of Tribology, **123**, pp. 205-210.

[19] Faria, M.T.C., and San Andrés, L., 2000, “On the Numerical Modeling of High-Speed Hydrodynamic Gas Bearings”, ASME Journal of Tribology, **122**, pp. 124-130.

[20] Hamrock, B. J., 1994, *Fundamentals of Fluid Film Lubrication*, McGraw-Hill, New York.

[21] Constantinescu, V. N., 1969, *Gas Lubrication*, the American Society of Mechanical Engineers, New York.

[22] Constantinescu, V. N., and Galetuse, S., 1976, “Pressure Drop due to Inertia Forces in Step Bearings”, ASME Journal of Lubrication Technology**, 98**, pp. 167-174.

[23] Foster, D. J., Carow, D., and Benson, D., 1969. “An Approximate Theoretical Analysis of the Static and Dynamic Characteristics of the Herringbone Grooved, Gas Lubricated Journal Bearing, and Comparison with Experiment”, ASME Journal of Tribology, **91**, pp. 25-32.

[24] Zirekelback, S., and San Andrés, L., 1998, “Finite Element Analysis of Herringbone Groove Journal Bearings: A Parametric Study”, ASME Journal of Tribology, **120**, pp. 234-240.

[25] Fonda, B.G., 2001, “Meruit Turbocompressor PRDA Task1: Gas Bearing Validation”, Personal communication. Meruit Inc., Santa Monica, CA.

[26] Ajayi, O. O., Woodford, J. B., Erdemir, A., and Fenske, G. R., 2002, “Performance of Amorphous Carbon Coating in Turbocompressor Air Bearings”, Society of Automotive Engineers, 2002-01-1922, pp. 1-4.

[27] Sastri, S., Gunda, N., Cooke, R., Jha, S. and Desai V., 2001, “High Performance DLC Coatings for Severe Wear Applications”, Personal communication. Surmet Inc., Burlington, MA.

[28] Dellacorte, C., Fellenstein, J. A., and Benoy, P. A., 1998, “Evaluation of Advanced Solid Lubricant Coatings for Foil Air Bearings Operating at 25 and 500°C”, NASA/TM-1998-206619, pp. 1-10.

[29] Stowell, T. B., 1971, “Pneumatic Hammer in a Gas Lubricated Externally Pressurized Annual Thrust Bearing”, ASME Journal of Lubrication Technology, **93**, pp. 498-503.

[30] San Andrés, L., and Childs, D., 1997, “Angled Injection-Hydrostatic Bearings Analysis and Comparison to Test Results”, ASME Journal of Tribology, **119**, pp. 179-187.

[31] Czolczynski, K., 1999, *Rotordynamics of Gas-Lubricated Journal Bearing System*, Springer, New York.

[32] San Andrés, L., and Wilde, D., 2001, “Finite Element Analysis of Gas Bearings for Oil-Free Turbomachinery,” Revue Européenne des Eléments Finis, **10 (6/7)**, pp. 769-790.

[33] Wilde, D.A., and San Andrés, L., 2003, “Comparison of Rotordynamic Analysis Predictions with the Test Response of Simple Gas Hybrid Bearings for Oil Free Turbomachinery,” ASME Paper No. GT 2003-38859, pp. 1-14.

[34] Wilde, D., 2002, “Experiment Response of Gas Hybrid Bearings for High Speed Oil-Free Turbomachinery”, Mechanical Engineering M.S. Thesis, Texas A&M University, College Station, TX.

[35] XLTRC/XLTRC^2 Rotordynamic Software Suite, 2003, Turbomachinery Laboratory, Texas A&M University, College Station, TX.

[36] Vance, J. M., 1988, *Rotordynamics of Turbomachinery*, John Wiley & Sons, New York.

[37] San Andrés, L., 2003, “Finite Element Program for Rayleigh Step Bearing”, Personal communication, Texas A&M University, College Station, TX.

[38] Lund, J. W. 1968, “Calculation of Stiffness and Damping Properties of Gas Bearings”, ASME Journal of Lubrication Technology, **90**, pp. 793-803.

APPENDIX A

ROTOR COASTDOWN SPEEDS ON ITS BEARINGS FOR VARIOUS FEED GAS PRESSURES

The applied NFC coating on the rotor surface provides low friction against its bearings. The coating on the rotor was intact before conducting tests with bearing set #1. Figure A.1 shows the coastdown speeds at various feed gas pressures on this test bearing pair. All coastdown tests started from 20 krpm. For speeds above 80% of the initial speed, the rotor decelerates at the same rate for each feed pressure. Note that increasing supply gas pressure slows the speed decay for speed ratios below 0.6, thus extending the rotor touchdown time on its bearings. The rotor speed drops quickly from the speed ratio below ~ 0.4 (8,000 rpm). Dry friction (rubbing) happens below ~ 20% of the top speed, i.e., 4,000 rpm, as the gas film is not adequate to support the rotor, as shown in Figures 8-10. The rotor probably shows operation with viscous drag at first (above speed ratio of ~ 0.5), and then transitioning to dry friction once rubbing occurs.

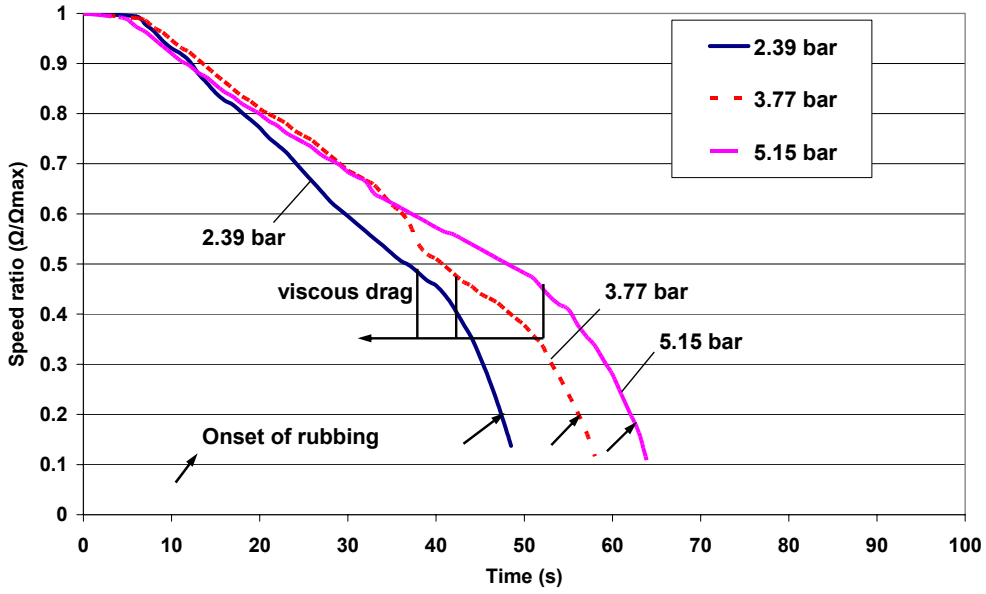

Fig. A.1 Rotor coastdown speed ratio versus time for Rayleigh step bearing set #1 for various feed gas pressures

After conducting the tests with bearing set #1, the NFC coating on the rotor was damaged and removed most from the rotor surface. Subsequent tests were performed with bearing set #2. Figure A.2 show the rotor coastdown speeds at various feed pressures from a top speed of 14.5 krpm. Similarly, the rotor shows more time to decelerate for a higher feed gas pressure since the pressurized air decreases the shaft eccentricity (assist to lift the rotor). Note the rotor coasts down more rapidly on this bearing pair as compared to the bearing set #1. For example, 12 seconds and 30 seconds are required respectively for bearing set #2 and set #1 when the rotor speed decays to 60% of the initial speed for a feed pressure of 2.39 bar. Rubbing starts from the speed ratio ~ 0.3 (~ 4,300 rpm), also shown in Figure 19.

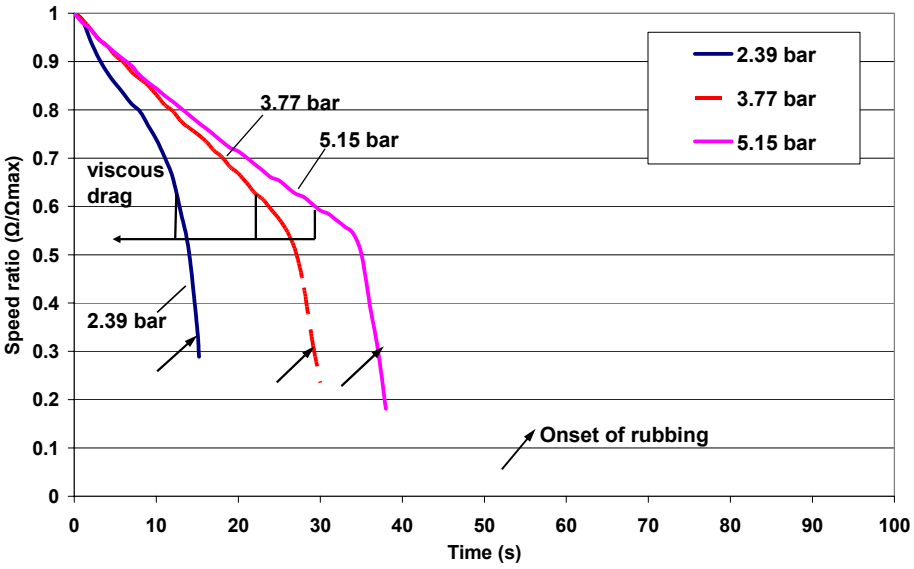

Fig. A.2 Rotor coastdown speed ratio versus time for Rayleigh step bearing set #2 for various feed gas pressures.

Earlier tests of a Teflon coated rotor supported on flexure pivot tilting pad bearings (FPTPBs) [7] show a very different coastdown speed behavior. Figure A.3 presents the rotor coastdown speed ratio versus time from a top speed of 30 krpm. A higher feed pressure provides a low friction on the rotor for speed ratios below ~ 0.2 (6,000 rpm), extending the rotor landing time at its bearings. Note the rotor takes 80

seconds to slow down to 20% of the top speed for the feed pressure of 5.15 bar, more than with the Rayleigh step bearing which require only 60 seconds to reach the same speed ratio at the feed pressure of 5.15 bar, shown in Figure A.1. The rotor on the FPTPB behaves like a viscous drag model.

In general, the coating on the rotor surface is useful to reduce the rotor friction against its bearing at liftoff and touchdown. The Flexure pivot tilting pad bearings (FPTPBs) show much lower friction than the Rayleigh step bearings, more evident at low shaft speeds. The rotor decelerates slowly on the FPTPBs.

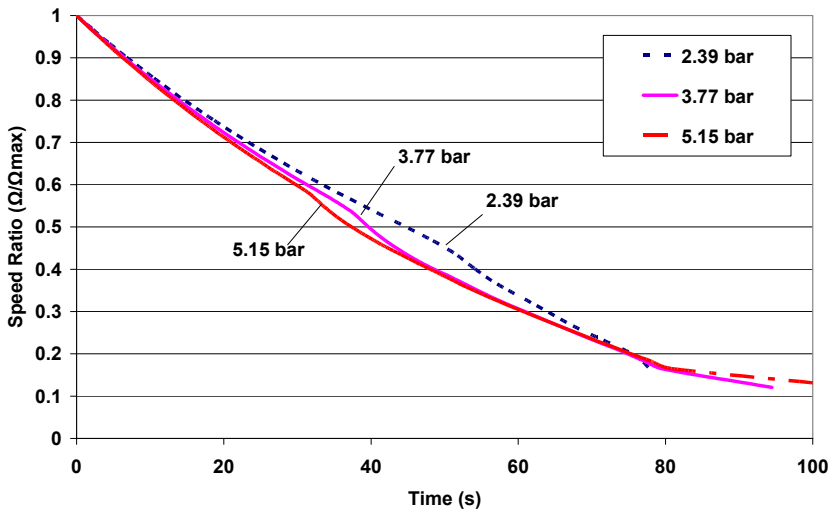

Fig. A.3 Rotor coastdown speed ratio versus time for flexure pivot bearings with 20 µm radial clearance at various feed gas pressures

VITA

Xuehua Zhu was born in Sichuan, China on March 10, 1974. She received her Bachelor of Science degree in mechanical engineering from the Power Machinery Engineering Department at Xi'an Jiao Tong University in July 1996. After graduation, she worked for Shanghai Blower Works in the design department. In 2000, she joined Atlas Copco (Shanghai) Trading Company as a technical support engineer in the marketing department. Xuehua completed her graduate study in August 2004, under the guidance of Dr. San Andrés at Texas A&M University.

Permanent Mailing Address:

Xuehua Zhu
4-402, 999 San Quan Road
Shanghai, 200435
People's Republic of China